

## Review

# A comprehensive study of various superconductors for superconducting nanowire single photon detectors applications

Sangita Tripathy,<sup>1,3</sup> Kriti Tyagi,<sup>1,2,3,\*</sup> and Pratiksha Pratap<sup>1,2</sup>

## SUMMARY

**Research activities in the field of superconducting nanowire single photon detectors (SNSPDs) have exhibited major progress over the last two decades. The low dark count rate, low jitter time, low recovery time, and ultrafast response time in an extended wavelength range, along with several improvements in the material parameters, cryogenic environment, and associated electronics make SNSPDs a superior choice over other photo-detectors. The struggle in simultaneously optimizing these parameters made the pace of SNSPD research steady, until the report of unit system detection efficiency at low temperatures for WSi SNSPD. Due to the difficulty in maintaining the low temperature for a long time, researchers are currently focusing on using high transition temperatures cuprate-based superconductors. These have the added advantages of making a portable SNSPD combined with faster response dynamics required for commercial SNSPD applications. In this review, we have discussed different models for single photon detection, followed by research activities carried out employing different superconducting materials over the last 20 years. The ongoing research toward utilizing oxide-based superconductors as photon detection devices along with a few suggestions for improving the device performance is discussed. This review will fill the gap required for a detailed study of different classes of superconductors for SNSPD applications.**

## INTRODUCTION

The superconducting single photon detectors (SNSPDs) have captured significant scientific interest over the last two decades through their unique capability of cooper pair breaking by photon absorption. The advantages such as high efficiency, extremely low dark count rates, short timing jitter, fast recovery time with no after-pulsing, and enhanced sensitivity from ultra-violet to infrared region, makes SNSPD superior over their counter parts, such as; superconducting tunnel junctions (STJ), photo multiplier tubes (PMT), transition edge sensors (TES), semiconducting avalanche photo-diodes (SPAD), and superconducting hot-electron bolometers (HEB).<sup>1,2</sup>

### Significance of superconducting single photon detector devices

The research on implementing superconductors as light detectors started with the remarkable discovery of the destruction of superconductivity in lead (Pb) films by Laser radiations, the physics of which could not be explained by simple resistive heating.<sup>3</sup> The basic working principle behind SNSPDs was derived from the concept of radiation bolometers fabricated from semiconducting and superconducting thin films.<sup>4</sup> Goltzman et al. fabricated 1 μm long, 0.2 μm wide, and 5 nm thick niobium nitride (NbN) nanowire-based SNSPD device using a visible light of 810 nm wavelength as the photon source.<sup>5</sup> The schematic operation of a typical SNSPD is shown in Figure 1. Here, the polarization controller plays a key role in forwarding polarized photons, the attenuator controls the average number of photons in a light field, the cryocooler maintains the necessary temperature for photon detection, and the bias tee passes the DC bias current to the device and AC signal from the device back to the amplifier. The oscilloscope or photon counter finally counts and characterizes the output signal.<sup>6</sup>

The ultrahigh count rate (number of photons registered per unit time) in GHz, high detection efficiency (probability of converting absorbed photons into electrical signals) of >90%,<sup>7</sup> low dark count rate (false count rate which is not due to real photons) of  $10^{-4}$  Hz,<sup>8</sup> small jitter timing (uncertainty between receipt of photons and response at the output) of 4.6 ps,<sup>9</sup> and ultrafast reset time (time taken by the device to be ready for absorbing the next photon following signal detection at the output) of few ps<sup>10</sup> has uniquely established SNSPDs over their earlier competitors. This unique quantum technology has been effectively used in fields such as; quantum information science for secure data transmission,<sup>11,12</sup> quantum teleportation,<sup>13</sup> long-distance imaging and space communications (LIDAR),<sup>14,15</sup> astronomical rays detection in infrared

<sup>1</sup>CSIR-National Physical Laboratory, Dr. K.S. Krishnan Marg, New Delhi 110012, India

<sup>2</sup>Academy of Scientific & Innovative Research (AcSIR), Ghaziabad 201002, India

<sup>3</sup>These authors contributed equally

\*Correspondence: [kriti.tyagi@nplindia.org](mailto:kriti.tyagi@nplindia.org)

<https://doi.org/10.1016/j.isci.2024.110779>



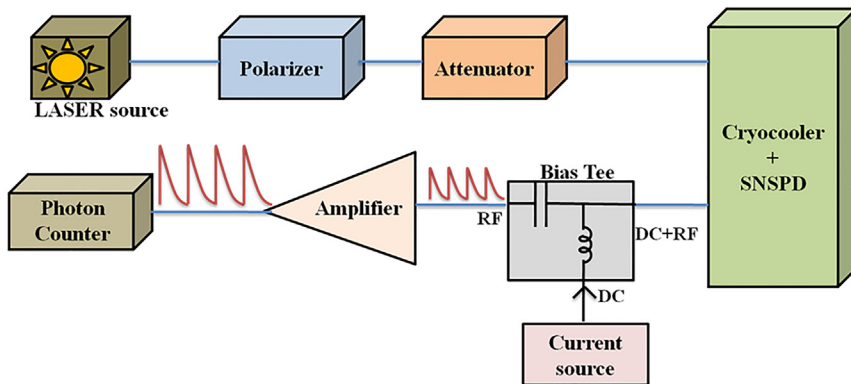


**Figure 1. Schematic diagram shows the operation of a typical SNSPD**

regime,<sup>16</sup> fluorescence spectroscopy for lifetime measurements of excited atoms using time-correlated photon counting,<sup>17</sup> and medical sciences for X-ray and CT scan imaging,<sup>18,19</sup> and so forth.

### Progress in superconducting single photon detectors devices

The analysis of current-voltage (I-V) curves obtained for different materials plays significant role in explaining the nature of photo-response. The sharp step in voltage for a given switching current (bolometric response) stands as a primary requirement for any material to be called an ideal photon detector. The mathematical expression is given by<sup>4</sup>:

$$\delta V = IR_0 \left[ \frac{1}{R_0} \left( \frac{dR}{dT} \right) \right] \delta T$$

where  $\delta V$  and  $\delta T$  represent changes in voltage and temperature,  $I$ ,  $R_0$ , and  $\frac{dR}{dT}$  represent the current, resistance, and temperature dependant resistance change for the material, respectively.

The successful response from NbN devices<sup>20</sup> encouraged different research groups to study and improve the device parameters in other nitride-based SNSPDs in terms of active area geometry, coupling to the optical source, cryogenic environment, and associated electronics.<sup>21,22</sup> The niobium titanium nitride (NbTiN),<sup>23</sup> tantalum nitride (TaN),<sup>19,24</sup> molybdenum nitride (MoN),<sup>25</sup> and vanadium nitride (VN) (exhibited unit intrinsic detection efficiency)<sup>26</sup> based devices have been successfully used as SNSPDs. The recently developed NbTiN-based devices have been reported of 99.5% intrinsic detection efficiency. Among silicon-based materials, NbSi<sup>27</sup> and MoSi<sup>28</sup> have successfully responded to infrared photons with detection efficiencies of 98% in the later.

The cuprate oxide-based SNSPDs with their faster breakdown and recombination dynamics of quasi-particles compared low  $T_C$  superconductors have gathered scientific interest in the SNSPD community. They tend to satisfy the growing demand for ultrafast response and quicker data transmission required in different fields.<sup>29</sup> They provide an option of using liquid nitrogen, a cheaper coolant compared to liquid helium, requiring lesser maintenance of the cryostat.<sup>30</sup> Therefore, cuprate oxide-based detectors create a prospect of economic and technological ease. The few underlying challenges for putting these devices for applications will be discussed in detail.

Figure 2 shows the progress in SNSPD research from the time of its inception in 2006 until now, which reflected a continuous progress. A few numbers of research publications and patents in the period of 2006–2010 indicated lack of scientific outlook in SNSPD research in initial days of its discovery. A visible rise in both publications and patents were noted in later years. Dauler et al. in 2014, reviewed the methods employed to develop fully packaged, high-performance SNSPDs along with the discussion about performance metrics of the fully developed SNSPD systems.<sup>31</sup> A detailed overview of the applications of SNSPDs was provided by Yamashita et al.,<sup>32</sup> You et al.<sup>12</sup> and Zadeh et al.<sup>33</sup> addressed the performance and other issues related with SNSPDs, in addition to their applications toward quantum information.

It is essential to consider material's inherent properties, cost and technical problems that arise during device fabrication, before choosing the superconducting material for SNSPD. There are closed-cycle cryostats that reach sufficiently low temperatures for the continuous operation of SNSPDs with excellent performance parameters, which are commercially available.<sup>35</sup> The high transition temperature superconducting materials are interesting, since, the phenomena of photon detection in high- $T_C$  materials provides a new approach to study the complex superconducting fluctuation phenomena. Secondly, they provide a technological solution for single-photon detection providing compact and cost-effective systems, which can use liquid nitrogen and enable mass deployment. The cuprate oxide superconductors occupy privileged position due to their layered structure and higher upper critical parameters. However, the larger band gap and difficulty in maintaining stoichiometric ratio at nano-dimensions hinders reaching desired transition temperature. The superconducting properties are degraded during nano-patterning, mainly due to phase fluctuations and altered oxygen stoichiometry. In the present review, we aim at summarizing the progress made, thus far, using numerous superconducting materials in the recent past toward SNSPD development. We have emphasized on role of dimensionality, patterning technique, and working environments for photon detectors, along with progress achieved so far in the same field.

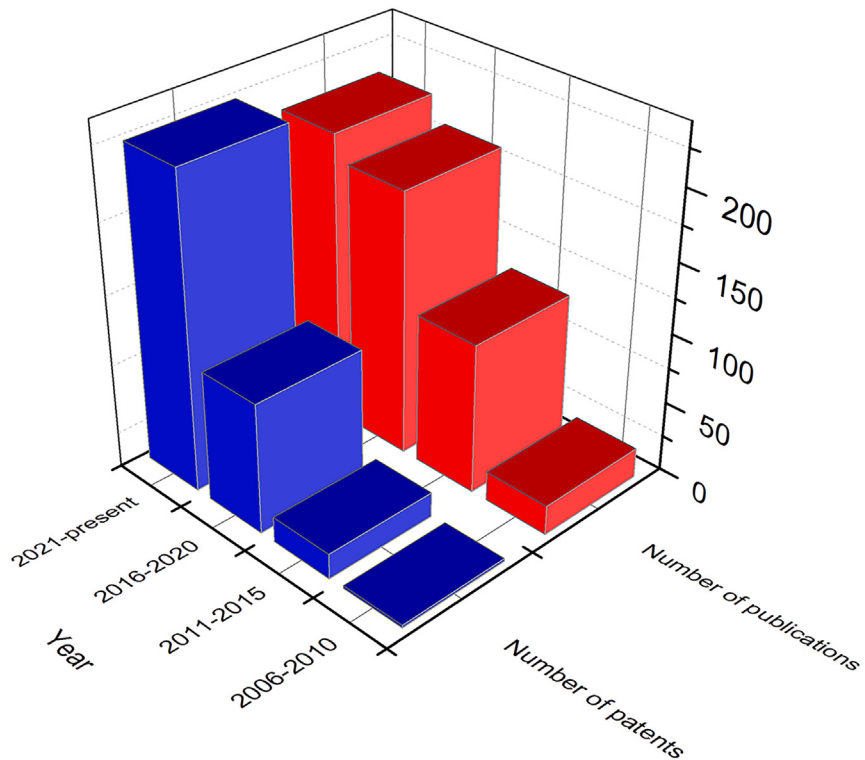


**Figure 2. Research papers and patents published in the area of SNSPD and related applications, since its inception**

### PHOTON DETECTION MECHANISM

The hysteretic I-V curve resulting upon the interruption of zero-voltage state of current conduction in an SNSPD device predicts its key parameters. Out of the few models proposed to understand the stepwise phenomena taking place during photon detection, two widely accepted models are<sup>36</sup>:

- (i) **Hotspot model** for high-energy photons
- (ii) **Vortex model** for lower energy photon

The widely accepted **Hotspot model** provides an easier way to understand the detection mechanism.<sup>37</sup> Here, the absorption of a visible or near-infrared photon breaks the cooper pairs locally with the generation of quasi-particles forming a local non-superconducting hotspot region (temperature >  $T_C$ ). A gradual rise in hotspot size toward both the sideways subsidizes the absorbed heat (Joule's heating effect). The bias current ( $I_B$ ) is to be maintained close to the critical current ( $I_C$ ) throughout the detection process. A voltage peak is detected at the output as the current across the wire-width exceeds  $I_C$ .<sup>5</sup> The quasi-particles follow a relaxation process through heat distribution to the surrounding by electron-electron, electron-phonon interactions, and heat dissipation to the substrate, in presence of low-temperature environment provided by the cryocooler.<sup>38</sup> The hotspot formation has been studied in terms of both thermal and electrical models. The thermal model uses the idea of time dependent heat balance equations<sup>2</sup>:

$$Cd\frac{\partial T}{\partial t} = J^2\partial\rho + \kappa d\nabla^2T + \alpha(T - T_0)$$

where,  $J$  is the current density and  $\rho$  is the electrical resistivity through the wire.

The electric model applies the concept of rise and decay times of the electrical signals, i.e., the nanowires are electrically represented as the series connection of an inductor  $L_K$  and a time dependent resistor  $R_n(t)$ , which is then parallelly connected to an external load ( $Z_0 \approx 50\Omega$ ). Here, the rise time and decay time are represented as<sup>39</sup>:

$$\zeta_1 = L_K / (Z_0 + R_n(t)) \text{ and } \zeta_2 = L_K / Z_0$$

Both thermal and electrical models provide straight forward explanation for the hotspot mechanism.

The **Vortex model** explains the photon detection process by BKT phase transition.<sup>40</sup> In this model, the magnetic vortices arising due to transport or bias current ( $I_B$ ) travel across the width of nanowires, provided  $I_B$  is lesser than critical current ( $I_B > I_C$ ) and temperature is lesser than theoretical value provided by BKT theory ( $T < T_{BKT}$ ).<sup>41</sup> The schematic representation of different mechanisms associated with vortex

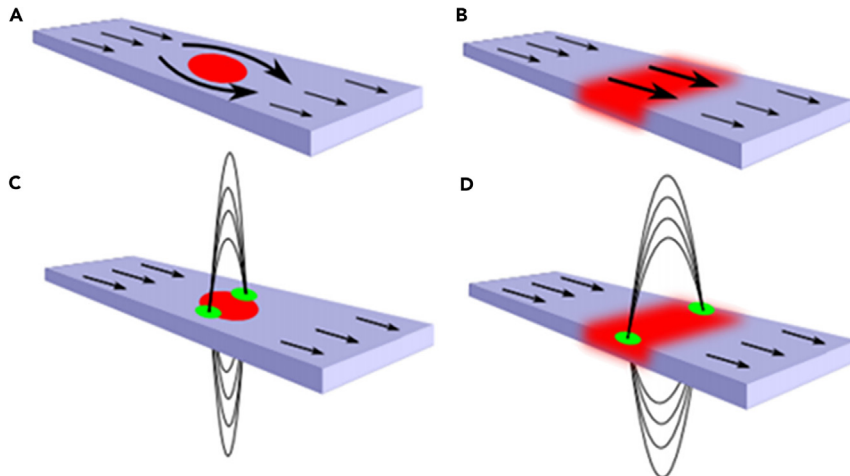


**Figure 3. Schematic representation of different mechanisms associated with vortex model in SNPSDs**

SNSPD detection models show (A) hotspot formation by the breaking of cooper-pairs, (B) spread in hotspot size, (C) vortex-antivortex depairing, and (D) vortex crossing from both edges of wire. Reproduced with permission.<sup>34</sup> Copyright 2014, American Physical Society.

model in SNPSDs is given in Figure 3.<sup>34</sup> The reduction in energy barrier for superconducting charge carriers finally gives rise to a resistive transition. The Lorentz force leads to the movement of vortex-antivortex pairs across the sideways.<sup>36</sup> The power-law dependence of applied voltage on current ( $V \sim I^3$ ) for  $T < T_{\text{BKT}}$  supports theory of vortex states arising due to topological defects.<sup>42</sup> However, the threshold values of energy and current for resistive transitions are dependent on dimension of devices. The phase slips in 1D quantum confinement Matsuda, Komiya,<sup>43</sup> vortex pair dissociation in 2D quantum confinements,<sup>44</sup> and vortex-antivortex pair formation in 3D quantum confinements<sup>42</sup> explains thermal, electrical, and quantum fluctuations to alter the superconducting states.

Altogether, the crystallinity and energy gap of the material, device geometry, and energy of photons play major role in deciding the photon detection model.<sup>36</sup> The THz radiations in infrared regime required to fulfill the long-distance communication requirements follow the vortex model, especially in high  $T_c$  superconductors.<sup>1</sup> It has also been confirmed through experiments using THz radiations in YBCO-based optical detectors.<sup>45,46</sup>

## DEVICE GEOMETRY AND PATTERNING EFFECTS

The geometry of device and dimensions (length, width, and thickness) of the patterned wire affect the superconducting properties and SNSPD device key parameters. Jiang et al. reported an ultrahigh  $J_c$  of  $10^9 \text{ A/cm}^2$  in 500 nm thick, 50 nm long, and 200 nm wide YBCO nanobridges patterned by UV photolithography.<sup>47</sup> The  $J_c$  was attributed to a uniform wire width, which was shorter than the transverse penetration depth ( $\lambda_L$ ). The dimension of superconducting wires also affects the efficiency and dark count rate of an SNSPD device. The kinetic inductance of the device ( $L_K = (\mu_0 \lambda^2)(L/A)$ ) also depends on length of wires, which in turn influences the jitter time and reset time of the SNSPD.<sup>36</sup> The jitter time and reset time were observed to reduce with decreasing length of the wires.<sup>48,49</sup> Hence, the length of superconducting wires requires to be optimized for fixed width and thickness. The reset time can be decreased by increasing the load impedance on the detector or by making use of parallel nanowire geometry to reduce the inductance. However, a decrease in detector efficiency due to latching effect was noted.<sup>50,51</sup>

The width of nanowires is vital, providing a defined path for the current flow. Any kind of fluctuation leading to phase slips are more probable in 1D wires ( $w < \lambda$ ,  $\lambda = 2\lambda_L^2/d$ ,  $\lambda_L$  = London penetration depth of material, and  $t < \xi$ ).<sup>44</sup> The wire width affects superconducting critical parameters such as  $T_c$ ,  $J_c$ , normalized resistance ( $R_N$ ), coherence length ( $\xi$ ), penetration depth ( $\lambda$ ), and transition width ( $\Delta T$ ). The oxygen loss during the patterning of ultra-narrow oxide wires leads to reduced superconducting parameters. Hence, the  $T_c$  and  $R_N$  values decrease with decreasing wire width.<sup>52,53</sup> The phase slips leading to the broadening of R-T curves fitted well with given equations for  $R_N$ , for wires width  $\ll 4.4\xi$ .<sup>54</sup> They also reported a non-linear change in superconducting parameters by varying width of YBCO wires, and the maximum  $J_c$  of  $10^8 \text{ J/cm}^2$  was noted for 95 nm wide wires.<sup>55</sup> The role of wire width for photon number resolution was analyzed by comparing 100–150 nm wide MgB<sub>2</sub> nanowires. The 100 nm wide wires detected both lower and higher energy photons, whereas, 150 nm wide wires could not resolve lower energy photons.<sup>56</sup> Marshili et al. fixed other parameters and varied wire widths, and reported difference in detection efficiency for 20 nm and 30 nm wide NbN wires.<sup>57</sup> The optimization of thickness is equally important for designing SNSPD device. Arpaia et al. observed non-thermal and non-bolometric response exhibited by 50 nm thick meander patterned YBCO wires to 1550 nm wavelength photons, which showed switching and recovery currents for 15 nm thick YBCO wires. It was attributed to the Joule's heating effect due to decreased thermal conductivity at reduced thickness.<sup>54</sup> The amount of doping in superconductors decides the c-axis length of unit cells and influences the electrical and thermal conductivity. High-quality uniform nanowires of optimum thickness are required for hysteretic I-V curves with bolometric response.<sup>58</sup> The microwires of NbN, MoSi, and WSi of 0.5–5  $\mu\text{m}$  width has shown photo-response to visible lights.<sup>26,59,60</sup> Thus,  $I_B$  and wire dimension plays

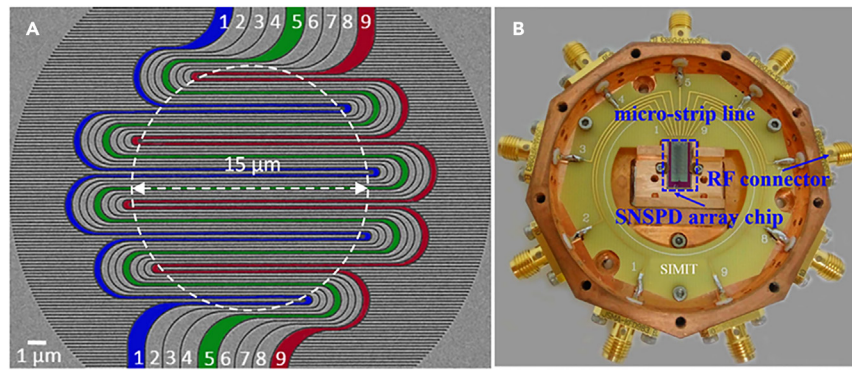


**Figure 4. Integrated nano-electro photonic device**

(A) SEM image of nine interleaved nanowire SNSPD array,<sup>75</sup> and (B) a chip mounting block holding SNSPD chip, Reproduced with permission.<sup>75</sup> Copyright 2018, IOP Science.

a crucial role here in approaching the required depairing current density. With decreasing thickness and increasing width of the microwires, the energy gaps is modified as per requirement for the detection of photons in wider wires.<sup>59</sup> The band gap can also be modified by the suitable concentration of dopant, following which dimensions can be optimized.<sup>61–63</sup>

The initially fabricated nano-bridge structures were followed by meander patterning in a rectangular or circular geometry, which maximized the region of active absorption. The idea of the meander pattern was modified to series + parallel ( $n+m$ ) geometries, where a set of ultrathin parallel nanowires were connected in series to the external load. Ejrnaes et al. suggested the (3 + 8) geometry for minimal latching and faster optical response.<sup>64</sup> The detectors designed with this kind of geometry lead to cascade switching, i.e., switching in one leading to switching in all, which results large amplitude of output signal due to the maximum absorption of photons.

## MATERIALS USED FOR SUPERCONDUCTING SINGLE PHOTON DETECTORS

### Nitride-based superconducting single photon detectors

#### Niobium nitride

The nitrides of transition metal possess various favourable characteristics such as high-melting point, hardness, abrasive resistivity and so forth and they are superconducting in nature.<sup>65,66</sup> Among the transition metal nitrides,  $\text{Nb}_3\text{N}_3$  and NbN are known to possess higher  $T_C$ .<sup>67</sup> The high  $T_C$  observed in these compounds coupled with stability observed at ambient temperatures makes them suitable for different superconducting device applications such as, single-photon detectors,<sup>68,69</sup> radio-frequency resonators<sup>70</sup> and bolometric mixers<sup>71,72</sup> and so forth. The presence of strong  $\text{N}\equiv\text{N}$  bond leads to small free energy of formation, thus, making the synthesis of nitrides difficult as compared to other counterparts e.g., oxides.

NbN has played a governing role in single-photon detection using superconducting nanowires. Goltzman et al.<sup>5</sup> demonstrated supercurrent assisted hotspot mechanism in ultrathin NbN strip employed for single photon detection in visible and infrared range. Consequently, QE of 20% was reported for  $0.81 \mu\text{m}$  photons with a negligible dark count. The response time corresponding to 10 GHz photon counting rate was measured to be  $\sim 100$  ps. Although different fabrication processes were used to produce NbN structures for single-photon detection, the recovery time has been underrated for long, owing to the kinetic inductance of the meander until 2006, when Rosfjord et al.<sup>73</sup> at Massachusetts Institute of Technology obtained high detection efficiency in NbN-based SNSPD. They added an optical cavity and anti-reflection coating to a nanowire photodetector, thus, creating an integrated nano-electro photonic device capable of showcasing enhanced performance as compared to the original device. As shown in Figure 4, the device was illuminated from the rear portion of the chip through the anti-reflection coating and the substrate. The photons that fail to get absorbed at NbN wire initially enter the optical cavity, thus, having a greater probability of being absorbed by NbN. The thickness of the optical cavity was chosen such that, the destructive interference leads to the a reduction of reflectance on the surface of NbN wire. The group reported a DE of 57% at 1550 nm and 67% at 1064 nm wavelength with a small pixel size of  $3.3 \times 3.0 \mu\text{m}^2$ . An important advancement made by Stern and Farr<sup>74</sup> has been to increase the pixel size ( $15 \times 15 \mu\text{m}^2$ ), so as to efficiently couple to fiber optic waveguide.

Based on the physics governing device operation, SNSPDs are known to achieve the required single-photon detection properties simultaneously. However, there are practical limitations involved in attaining them concurrently. The AC-coupled amplifier has to be attached to the readout signal. The amplifier, due to its non-linear interaction with the detector, limits the high-counting rates desirable for high efficiency in SNSPDs. Also, the small active area required to achieve lower kinetic inductance<sup>69</sup> ensures fast reset times and thus high count rates, however, this leads to strenuous optical coupling with high efficiency. The reset time can be reduced by either using a parallel nanowire configuration to decrease the inductance or by enhancing the load impedance of the detector. However, these attempts lead to a lower efficiency as a result of latching.<sup>76</sup> Owing to such conditions limiting the detector performance, Rosenberg et al.<sup>77</sup> stressed the system performance parameters that can be established simultaneously to gauge the advantages of SNSPDs for various applications. They discussed NbN-based

SNSPD system that can simultaneously achieve 68% detection efficiency at 1550 nm with a photon flux of 100 million pps, kHz noise count rates, and few kcps dark count rates along with a timing resolution of <80 ps.<sup>77</sup>

In 2016, Wu et al. reported the performance of SNSPDs deposited on MgF<sub>2</sub> substrate<sup>78</sup> to be comparable to other counterparts such as sapphire and MgO.<sup>79</sup> The choice of MgF<sub>2</sub> results owing to promising material properties such as wide bandgap, low refractive index, and wide optical transmission range. When compared to NbN, there is only a slight mismatch in the lattice constant. The mechanical strength and hardness of MgF<sub>2</sub> coupled with outstanding optical properties makes MgF<sub>2</sub> suitable for thin-film deposition followed by SNSPD fabrication. The front-side illuminated detector exhibited a system detection efficiency of 12.8% at a 100 Hz dark count rate while the backside illuminated SNSPD displayed 33% system detection efficiency at a similar dark count rate. The increase in efficiency with the addition of an optical cavity was attributed to enhancement in absorptance for the backside illuminated detector.

In addition to focusing on the physics regulating the device operation, several reports on improvement in the device design were recorded. For instance, by improving the NbN SNSPDs device design (i.e., devices with varied spacings of 80, 120, 160, 200, 240, 280, 320, and 360 nm having fill factor in the range 18–50%), Yamashita et al.<sup>80</sup> achieved a maximum system detection efficiency of 68.7% for moderate fill-factor of 18%. By concluding the simulation of the optical absorptance, they found that by appropriate tuning of the device design, high absorptance is achievable in the device, in spite of a low filling factor. In addition to the improvement in photon counting rate, a low filling-factor device design is believed to minimize complications in fabricating defect-free long nanowires. Similarly, Wang et al.<sup>81</sup> optimized NbN SNSPD design employing position-dependent detection efficiency. They proposed that: (1) The optimized device design of the meander wire NbN detector aids in boosting absorption by amending the field distribution across the length of the wire, and (2) The absorption at the edges can be improved by the deposition of a silicon nanowire atop of the superconducting nanowire. This practice enhances the total absorption efficiency and also the internal detection efficiency of the meandering wire pattern. Further integration of the proposed structure with a cavity structure makes it possible to achieve absorption efficiencies of 97% and 85% for perpendicular and parallel polarization, respectively. The polarization-sensitive absorptance of the nanowire leads to polarization-sensitive detection efficiency of the SNSPD meander. In order to resolve this problem, Huang et al. fabricated NbN SNSPDs having spiral structure and finally embedded in an optical cavity. The optical cavity combining spiral structure employed for the fabrication of SNSPDs removes the current crowding effect leading to a system detection efficiency of 52.5% at 1550 nm at a dark count rate of 100 Hz.

An approach was developed by Huang et al.<sup>75</sup> to increase the detection speed in NbN SNSPDs by replacing long individual nanowires with multiple single nanowires in an array. This arrangement led to a decrease in kinetic inductance and consequently rise in the count rate. They reported a detector with nine interleaved nanowires having 70% system detection efficiency at a dark count rate of 200 Hz and wavelength of 1550 nm. The SNSPD attained the highest count rate of 0.93 GHz at a system detection efficiency of 7% and an ability to resolve up to nine photons.

The variation of hotspot relaxation time  $\tau_{th}$  (a key factor that defines maximum count rate), for NbN-based SNSPDs, with parameters such as bath temperature, nanowire linewidth, type of substrate, and so forth were studied by Zhang et al.<sup>82</sup> They established that  $\tau_{th}$  enhanced with increase in bias-current, and a direct correlation between  $\tau_{th}$  and degree of disorder in NbN films deposited on various substrates was obtained.

In spite of the large number of investigations on QKD based on SNSPDs, the lower efficiency achieved in the initial years limited their widespread usage.<sup>73,83</sup> Hadfield et al.,<sup>84</sup> in 2006, integrated a cryogen-free SNSPD system that acts as a receiver in a fiber-based QKD link. They illustrated that by using the twin SNSPDs, it becomes possible to exchange a secure key over 12.2 dB link-loss, using the BB84 protocol. Tanaka et al.<sup>85</sup> successfully demonstrated QKD transmission at 625 MHz clock rate using 97 km field-installed fiber through practical clock synchronization using the same protocol. The QKD transmission system reported by Tanaka et al. entailed all the functions required<sup>86</sup> and thus, proved as a solid foundation for a complete QKD system.

Another important advancement was a demonstration of the first entanglement-based QKD experiment over 100 km optical-fiber.<sup>86–88</sup> For this, the researchers made use of different components, namely, (1) NbN-based SNSPDs, (2) an entangled photon-pair source consisting of fiber-coupled periodically poled lithium niobate waveguide coupled with ultra-low loss filters, and (3) Mach-Zehnder Interferometers. The combined effect of all components aided in the attainment of an entanglement-based QKD experiment over 100-km optical fiber, having a sifted key to 16 kbit and quantum-bit-error-rate of 6.9%, using BBM92 protocol. Making use of the progress experienced by SNSPDs and optical-fiber technology, Stucki et al.<sup>89</sup> implemented the COW protocol and reported a quantum key exchange spanning a distance of 250 km with 15 bits/s. Recently, NbN ultrathin films with incomparable homogeneity have been grown by atomic layer deposition (ALD) technique,<sup>90,91</sup> the use of which in SNSPD showcases saturated internal detection efficiency in the entire bias range. The sputtering technique used for the growth of epitaxial NbN thin films results in enhanced  $T_C$  and  $J_C$  and decreased resistivity values, as compared to polycrystalline films, however reduces device detection efficiency.<sup>92,93</sup> The growth by molecular beam epitaxy (MBE) leads to minimal defects in the grown epitaxial film and helps in achieving saturated detection efficiency. There have been reports on different nanofabrication techniques for NbN-based SNSPDs in the literature.<sup>94–96</sup> Korneeva et al. reported that a micron-wide NbN bridge would result in SNSPDs with appreciable count rate and enormous detection area.<sup>97</sup>

The superconducting properties of 4.5–7 nm thick Nb films fabricated for SNSPD applications were improved by a 1 nm thick aluminum nitride (AlN) capping layer. The 4.5 nm thick, 50 nm wide Nb/AlN devices exhibited a wide range of cut-off wavelength (1310–2010 nm), single-photon sensitivity, and enhanced detection efficiency (an order higher) for reducing the working temperature from 2.26 K to 315 mK.<sup>98</sup> Jia et al. deposited 30 nm thick Nb<sub>3</sub>N<sub>6</sub> buffer layer on 6 nm thick NbN thin film, deposited on silicon substrate. The  $T_C$  at zero-resistance state for the hybrid layers was 13.5 K, corresponding to a critical current density of  $10^7$  A/cm<sup>2</sup>. The  $J_C$  value was one order higher than that obtained

for bare NbN film, indicating the role of the  $\text{Nb}_5\text{N}_6$  buffer layer in raising the superconducting properties of ultrathin NbN film.<sup>99</sup> Xu et al. obtained enhanced superconducting properties in NbN thin film-based SNSPD devices fabricated on silicon substrates by using  $\text{Nb}_5\text{N}_6$  buffer layer. The  $T_c$  corresponding to a zero-resistance state for a 3 nm thick NbN film coated with a 20 nm thick buffer layer was 10.3 K, as compared to 7.4 K for bare NbN thin films. Moreover, the devices with  $\text{Nb}_5\text{N}_6$  buffer layer exhibited higher hysteresis current, lesser jitter time, and faster photo-response compared to bare NbN devices.<sup>100</sup>

### Niobium titanium nitride

With a view to improving detection parameters such as photon-counting rate and detection efficiency, researchers started studying other superconducting materials as a replacement to NbN. Dorenbos et al.<sup>101</sup> studied NbTiN as a potential candidate for SNSPDs, having critical temperature (15 K) and critical current density ( $5.8 \times 10^6 \text{ A/cm}^2$ ) comparable to NbN. The NbTiN-based detectors were fabricated on the silicon substrate, which allowed a straightforward integration in complex electronic circuits. The other advantages of Si substrate include the rectification of impedance matching problem and easier integration between the optical cavity and fiber coupling. The NbTiN SNSPDs exhibited low dark count rates while still matching the efficiency of NbN-based detectors, thus, resulting in an unmatched signal-to-noise ratio. However, these improved parameters could not collectively provide an improved detection efficiency (<0.5% at 960 nm). To improve the device performance of NbTiN-based SNSPDs, Miki et al.<sup>102</sup> prepared epitaxial NbTiN thin film on MgO substrate using load-lock reactive magnetron sputtering. They reported of device efficiency of 1.4% at 100 Hz and 25% lower kinetic inductance in NbTiN-based detectors as compared to NbN detectors. The authors hinted at the scope for further improvement in efficiency by optimizing the composition ratio of the NbTi target pellet. Similar to the work done by Dorenbos et al.,<sup>101</sup> Tanner and co-workers<sup>103</sup> used Si substrate for improved device performance. The group reported the performance of NbTiN-based SNSPDs contrived using oxidized silicon substrate in the wavelength ranging from 830 to 1700 nm. The highest efficiency at 1310 nm wavelength achieved with front-side illumination was published to be comparable to the outcome attained with the backside illumination process. The detection efficiency of 23.2% reported at  $\lambda = 1310 \text{ nm}$ , with the dark-count rate of 1 kHz coupled with improved reset times and low jitter timings established NbTiN-based SNSPDs as a suitable option for time-correlated single-photon counting experiments. In addition, response curves independent of the polarization effect were produced using a suitable averaging method. Zichi et al. focused on optimizing Nb and Ti concentration in 9 nm thick  $\text{Nb}_x\text{Ti}_{1-x}\text{N}$  superconducting thin films and reporting of the best critical parameters at  $x = 0.62$ . The device fabricated of 20  $\mu\text{m}$  active area and operated at 2.5 K temperature exhibited its optimum detection efficiency (80%) at 1550 nm wavelength at 2.5 K. A jitter time of 19.5 ps was noted.<sup>104</sup>

Besides the investigation of the type of substrate material suitable for improving the detection efficiency of NbTiN-based SNSPDs, the optimization of device design helps to achieve efficient detectors suited for applications such as time-domain reflectometers<sup>105</sup> and quantum cryptography.<sup>106,107</sup> Schuck et al.<sup>108</sup> studied a variety of detector designs and probed the noise performance of such detectors. The NbTiN-based SNSPDs were patterned directly on top of  $\text{Si}_3\text{N}_4$  waveguides. Jia et al.<sup>109</sup> showed that by increasing the composition of Ti to double the value as used for usual NbTiN films, lattice-mismatch, and low resistivity can simultaneously be enhanced thus, improving the efficiency of NbTiN-based SNSPDs. For applications such as laser ranging and quantum computing, that consist of non-idealistic photons, it becomes crucial to improve the timing resolution of the detectors. The 8–13 nm thick NbTiN-based SNSPDs fabricated by Gourguès et al. exhibited system detection efficiency values of 64% and 82% for Laser wavelengths of 1550 nm and 785 nm, respectively, and 100% internal detection efficiency in the visible spectrum, for devices operated at 2.5 K operating temperature.<sup>110</sup> To achieve unparalleled timing resolution, Zadeh et al.<sup>111</sup> optimized the custom readout electronics followed by fixing it inside a cryostat at the 30K stage. The group demonstrated a device consisting of high efficiency, low-timing jitter, low dark-count rate, and high photon-detection rates. The device performance of SNSPDs based on material with a low superconducting energy gap was thought to provide high detection efficiency even in the case of low-energy incident photons. The same group fabricated an 8–11 nm thick NbTiN-based SNSPD device and reported a jittered time of 7.7 ps (10–16 ps range), and system detection efficiency of 80–90% in 780–1000 nm and 1310–1550 nm wavelength range.<sup>112</sup> Chang et al. fabricated NbTiN-based SNSPDs on  $\text{SiO}_2$  membranes by sputtering, and meander nanowires were patterned by EBL. The devices exhibited 94%–98% system detection efficiency with 15–26 ps jitter time at 2.7 K temperature when shined with 1260–1625 nm wavelength photons. Their best detection parameters obtained were the detection efficiency of 99.5% (jitter time of 35 ps) for 1350 nm photons.<sup>113</sup> Chang et al. also obtained more than 70% system detection efficiency and less than 15 ps jitter time with 40–60 nm wide, 7.5–9.5 nm thick NbTiN-based SNSPD devices operated at 2.5 K temperature, and shined with 2  $\mu\text{m}$  wavelength Laser lights. The observance of 100% and 80% internal detection efficiencies at 3 and 4  $\mu\text{m}$  Laser wavelength, respectively, indicated their efficiency to function in the mid-infrared range with very good time resolution.<sup>114</sup> The role of polarizability of incoming photons on the efficiency of fiber-coupled NbTiN SNSPD detectors fabricated over 20, 25, and 50  $\mu\text{m}$  diameter cross-sectional areas were studied by Chang et al. for visible, near-infrared, and telecom wavelength photons. A more than 80% system detection efficiency was noted for 20  $\mu\text{m}$  wide device, whereas, a 70% efficiency was obtained for 50  $\mu\text{m}$  wide device, with a jitter time of sub 20 ps for all the devices. Also, a polarization dependency for NIR and telecom wavelength was observed in the devices, which increased for increasing photon wavelengths.<sup>115</sup> The 50–100 nm wide  $\text{Nb}_{0.15}\text{Re}_{0.85}$  nanowires with meander structure covering a circular detection area of 10–16  $\mu\text{m}$  area showed a recovery time of 8–19 ns and a jitter time of 35 ps at the readout circuit when illuminated with 1301 nm wavelength light and operated at 2.8 K temperature.<sup>116</sup>

### Other nitrides (tantalum nitride, molybdenum nitride, and vanadium nitride)

For TaN, excluding  $T_c$  and superconducting energy gap, both being appreciably smaller, most of its considerable parameters match those of NbN. Due to the smaller superconducting gap, TaN-based SNSPDs were thought of as a potential alternative to NbN SNSPDs in infrared and

near-infrared regimes. Owing to their hardness and chemically inert nature, nitride compounds are used mainly for mechanical and micro-electronic applications.<sup>117,118</sup> A fine tailoring of the stoichiometry in nitride compounds by varying deposition conditions leads to variation in the properties of nitrides (ranging from insulator to superconductor). K. Il'in et al.<sup>119</sup> fabricated ultra-thin films of TaN and discussed their normal and superconducting properties with an aim to employ TaN material for SNSPD device fabrication. The transition temperature of 5 nm thick TaN film patterned into a meander structure with 110 nm width was reported to be 8.3K, having a critical current density of 4 MA/cm<sup>2</sup> at 4.2 K temperature. Such SNSPDs demonstrated 20% detection efficiency at wavelength <700 nm. Engel et al.<sup>120</sup> showed that TaN-based SNSPDs recorded improved detection properties at higher wavelengths as compared to NbN-based detectors. A detection model that takes into account the quasi-particle multiplication and diffusion was employed to describe TaN-based detector performance. TaN devices recorded the optimum, temperature-independent performance at ~2K. Engel and co-workers took TaN-based SNSPD research further by studying the temperature dependency of detection efficiency in NbN and TaN-based SNSPDs.<sup>121</sup> They found that the detectors having significant inhomogeneities are capable of achieving high efficiencies when operated at low temperatures. Korneeva et al. reported that the hot-spot formation over a larger area in MoN-based SNSPD resulted in saturated detection efficiency at a wavelength of 1064 nm.<sup>122</sup> Similarly, a T<sub>C</sub> value of 9 K for VN-based SNSPD with saturated detection efficiency at 900 nm was reported by Evtikhiev and Rodin.<sup>123</sup>

### Silicon-based devices

#### WSi

Despite of other parameters improved in NbN-based SNSPD devices in quantum optics measurements,<sup>106,124,125</sup> the low system detection efficiency<sup>126</sup> limits its use for photon detection applications. The low efficiency could be due to various reasons. Firstly, polycrystalline NbN offers a lesser degree of freedom in the optimization of optical coupling and detector absorption. Secondly, the internal detection efficiency of NbN-based SNSPDs does not show saturation with bias current. The crystal structure of NbN films determines its superconducting properties.<sup>127</sup> Thus, NbN films cannot be employed for use in large-area device fabrication.<sup>128</sup> This sets a limitation on the choice of substrate and also the design parameters for optical structures to be used for the enhancement of absorption in NbN nanowires. The amorphous superconductors are predicted to offer various advantages over NbN and NbTiN-based detectors. In amorphous materials the superconducting gap energy is low, thus, providing a higher intrinsic detection efficiency at longer wavelengths. The substrate requirements are not strict and they can be used with a variety of substrates. The free carrier concentration in amorphous superconductors is low, which leads to low critical current densities and hence a large hotspot size in the event of absorption of an incident photon.<sup>129</sup>

WSi has been investigated as an alternative material by the group at the National Institute of Standards and Technology, USA. Baek et al.,<sup>129</sup> in 2011, developed WSi-based SNSPD with a detection area of 16 × 16 μm<sup>2</sup> and saturated internal quantum efficiency in the wavelength range from visible to 1850 nm. WSi was predicted to overcome the limitations posed by NbN nanowires, thus leading to the fabrication of highly efficient WSi-based SNSPDs. Marsili et al.<sup>130</sup> reported that WSi nanowires have a number of advantages over NbN and NbTiN nanowires and that WSi nanowire-based SNSPDs approach the ideal performance of single-photon detectors. The nanowires of WSi are robust with respect to structural defects, providing enhanced compatibility with the structures that aided in enhancing detector absorption and optical coupling, easily deposited on a variety of substrates and WSi-based SNSPDs have shown saturated detection efficiency with respect to the bias current I<sub>B</sub>,<sup>129</sup> in near-infrared region.

Recently, great advancement has been attained in the improvement of SNSPD device efficiency.<sup>130</sup> The detection efficiency of the WSi-based device upon integration with the optical cavity was found to be greater than 90% in the wavelength range of 1520 nm–1610 nm. The parameters that led to exceptional efficiency are dark-count rate (~1 cps), timing jitter (~150 ps), and reset time (40 ns). The achievement of a high detection efficiency in WSi was related to the intrinsic photon detection mechanism observed in an SNSPD device.<sup>131</sup> The small superconducting energy gap of WSi coupled with low carrier density as compared to materials such as NbN, led to the creation of a large number of quasi-particles per each absorbed photon. In addition to the rise in detection efficiency, the operation of WSi SNSPDs was also investigated at 2.5K (70% of its T<sub>C</sub>). Verma et al.<sup>132</sup> showed that, at 2.5K, the detection efficiency saturated at 78 ± 2% at 1310 nm wavelength. The high efficiency achieved at temperatures extremely close to critical temperature emerged to be a distinctive characteristic of WSi. Despite the favorable value of efficiency, the jitter time was found to be ~191 ps. This increased jitter time was an outcome of noise in the readout, which can be improved by making use of cryogenic amplifiers. WSi-based SNSPDs were also employed for deep-space optical communication.<sup>133</sup> Allmaras et al.<sup>133</sup> developed a 64-pixel array of WSi SNSPD, with a diameter array of 320 m, to be used as a ground receiver.

#### Molybdenum silicide

Despite of a large number of materials studied for SNSPDs, a material with optimum detection parameters was still been searched for. For some materials, the T<sub>C</sub> was reported to be too low. Nanowire fabricated from a 4.5 nm WSi film had a T<sub>C</sub> of 3K<sup>129</sup> and required to be operated below 1K in order to achieve a high detection efficiency. In WSi-based detectors, saturation in internal detection efficiency was observed only at temperatures below 2K at 155 nm wavelength, with a critical current value as low as 2 μA at 2K. The highest efficiency obtained to date is 93%, with a restriction of operating temperatures near 120 mK. The NbSi-based SNSPDs showed T<sub>C</sub> of ~2K.<sup>134</sup> Korneeva et al.<sup>135</sup> studied SNSPDs based on metal-silicon alloy, MoSi, having T<sub>C</sub> values higher than those of WSi and NbSi. A 25 nm thick Mo<sub>0.75</sub>Si<sub>0.25</sub> film was reported to have a T<sub>C</sub> of 7.5 K,<sup>136</sup> while a 50 nm thick Mo<sub>0.80</sub>Si<sub>0.20</sub> film had T<sub>C</sub> of 7.3 K.<sup>137</sup> The bulk superconducting energy gap for Mo<sub>0.75</sub>Si<sub>0.25</sub> film is 2.28 meV which is less than half the gap of NbN (4.9 meV). Thus, MoSi-based SNSPDs were believed to provide higher critical temperatures as compared to WSi, which requires an expensive and complicated cooling system to achieve optimum performance at temperatures below

1 K. The MoSi thin films have  $T_C$  values > 4K, thus, MoSi-based SNSPDs could be operated at temperature >2K, employing economic, less complex, and efficient closed cycle cryogenic systems.<sup>138</sup>

Korneeva et al.<sup>135</sup> fabricated SNSPDs based on 4 nm thick  $\text{Mo}_x\text{Si}_{1-x}$  thin films with 25% and 20% Si content i.e.,  $\text{Mo}_{0.75}\text{Si}_{0.25}$  and  $\text{Mo}_{0.80}\text{Si}_{0.20}$ , respectively. The electrical resistivity for  $\text{Mo}_{0.75}\text{Si}_{0.25}$  and  $\text{Mo}_{0.80}\text{Si}_{0.20}$  films at 10 K were 220  $\mu\Omega$  and 185  $\mu\Omega$ , respectively. The higher  $T_C$  of  $\text{Mo}_{0.80}\text{Si}_{0.20}$  led to higher critical current in these devices as compared to devices made from  $\text{Mo}_{0.75}\text{Si}_{0.25}$ . A 7  $\mu\text{m} \times$  7  $\mu\text{m}$  detector demonstrated a 1/e voltage decay time (6 ns) limited by kinetic inductance. The timing jitter (120 ps) was found to be restricted by amplifier noise RMS. The highest detection efficiency value of 18% was achieved at 1.2  $\mu\text{m}$  wavelength. The MoSi-based SNSPDs allowed integration with optical cavities, thus allowing front-side illumination, and were predicted to have high potential for SNSPD development.

An attempt to increase the performance of MoSi SNSPDs was reported by Verma et al. The device was embedded inside an optical stack to enhance the absorption at 1550 nm wavelength.<sup>139</sup> The highest efficiency of  $87.1 \pm 0.5\%$  at 1542 nm, with a timing jitter of 76 ps was obtained at a temperature of 0.7 K. These SNSPDs were observed to showcase high saturated internal efficiency even at temperature as low as 2.3 K. Their polarization dependence was 2.8% with a linear dependence of count rate on input photon flux. The devices at 2.3 K exhibited performance comparable to WSi-based SNSPDs at <1 K and thus, limited the use of complex cryogenics. The potential candidature of MoSi thin films for SNSPD applications was further confirmed by Li et al.<sup>140</sup> wherein, the detailed low-temperature nano-optical studies of silicon-on-insulator waveguide integrated MoSi SNSPD were carried out. The MoSi-based devices qualified for on-chip single-photon detection in optical quantum information processing. The authors combined the advantages of MoSi-based device and traveling wave SNSPD design. A hair-pin-shaped MoSi-based SNSPD device was fabricated atop a single-mode SOI waveguide. The integration of the waveguide with MoSi-SNSPD leads to a high light absorption rate. The uniformity of the MoSi hairpin device was confirmed via photo-response mapping. The high  $T_C$  of MoSi-based SNSPDs coupled with large critical current indicated that those devices could exhibit improved performance at  $\sim 2.5$  K.

Banerjee et al.<sup>141</sup> carried out a comprehensive study of various properties of MoSi thin films toward SNSPD applications. A  $T_C$  of 5.5 K and a critical current density of 0.36 MA/cm<sup>2</sup> for 5 nm thick film at 3.6 K demonstrated that MoSi nanowires can be employed for SNSPD applications even at elevated temperatures. The prime motive of the work was the optimization of MoSi nano-films for realizing uniform large-area SNSPD focal-plane array and integration with advanced optical architecture. In order to optimize SNSPDs to work under 400 nm wavelength range, Wollman et al.<sup>142</sup> designed SNSPDs working in the wavelength range of 250–370 nm and termed them as UV SNSPDs. The MoSi-based UV SNSPDs possessed the capability to operate at temperatures as high as 4.2K. The active area of these detectors was 56  $\mu\text{m}$  diameter with a timing resolution of 60 ps (FWHM), dark count rate of  $\sim 0.25$  cps, and efficiency range of 70–80% and they were non-responsive to visible and infra-red photons. These parameters established MoSi-based UV SNSPDs as suitable candidates for applications such as UV fluorescent lifetime imaging microscopy, LIDAR, trapped-ion quantum-information processing, and photon-starved UV astronomy.

### NbSi

The efficiency of SNSPDs was moderate in the visible spectrum range and dropped significantly for wavelengths above 1  $\mu\text{m}$ . The use of optical cavities was an efficient way of enhancing the efficiency in the infrared range.<sup>73</sup> However, this approach became inapplicable for photons with energy lesser than that required to induce a detection event. With an aim to achieve high efficiency in the near-infrared range, Dorenbos et al.<sup>134</sup> fabricated NbSi-based SNSPD and compared its characteristics with NbTiN-based device. A 10 nm thick layer of  $\text{Nb}_{0.48}\text{Si}_{0.52}$  was deposited on oxidized silicon using a co-sputtering technique. The critical temperature reported for 10 nm thick  $\text{Nb}_{0.48}\text{Si}_{0.52}$  film was  $\sim 2$  K. The detection efficiency of the NbSi detector was ten times higher as compared to NbTiN-based detector when measured in the 1100–1900 nm wavelength range. In order to record a direct comparison of the sensitivity, both NbSi and NbTiN detectors were placed in close vicinity and an optical fiber was staged atop the detectors such that, both the detectors were illuminated with approximately same intensity. The critical current value of NbSi SNSPD was measured to be 2.2  $\mu\text{A}$ . It was further predicted that high detection efficiency at infrared wavelength was enhanced by improving the NbSi detector geometry followed by fiber coupling.<sup>103</sup>

### MoGe

A high detection efficiency was achieved in WSi-based SNSPD, along with the observation of a large timing jitter. The critical current in WSi was lower as compared to NbN, thus, leading to a low signal-to-noise ratio and consequently higher timing jitter.<sup>129,143,144</sup> The  $T_C$  of WSi SNSPD was nearly 3K, which required operation below 1 K for obtaining the desired system detection efficiency. However, operation at such low temperatures requires expensive and specialized cryogenic equipment. Verma et al.<sup>131</sup> fabricated SNSPD based on amorphous  $\text{Mo}_{0.75}\text{Ge}_{0.25}$  and noticed that the superconducting gap in MoGe was adequate to carry out the operation of SNSPD close to 2.5K, but low enough to yield a hotspot size sufficient enough to be able to produce saturated internal detection efficiency even for wider nanowire geometries. The deposited  $\text{Mo}_{0.75}\text{Ge}_{0.25}$  films of 7.5 nm thickness were deposited on the Si wafer using DC magnetron sputtering.

The system detection efficiencies of nanowires with 110 nm and 150 nm widths are shown in Figure 5. A greater than 20% detection efficiency along with a timing jitter of 187 ps was noticed at temperatures close to 2.5K. The efficiency of MoGe-based SNSPD could be further improved by embedding it inside an optical stack alike its WSi counterpart. The MoGe-based SNSPDs exhibited improved detection parameters as compared to WSi SNSPDs. Over the entire bias range, the dark count rate for MoGe SNSPDs was <500 cps, as compared to  $\sim 1000$  cps for WSi detectors. The phenomenon of latching observed for WSi SNSPDs led to lower recovery time as compared to MoGe. The higher

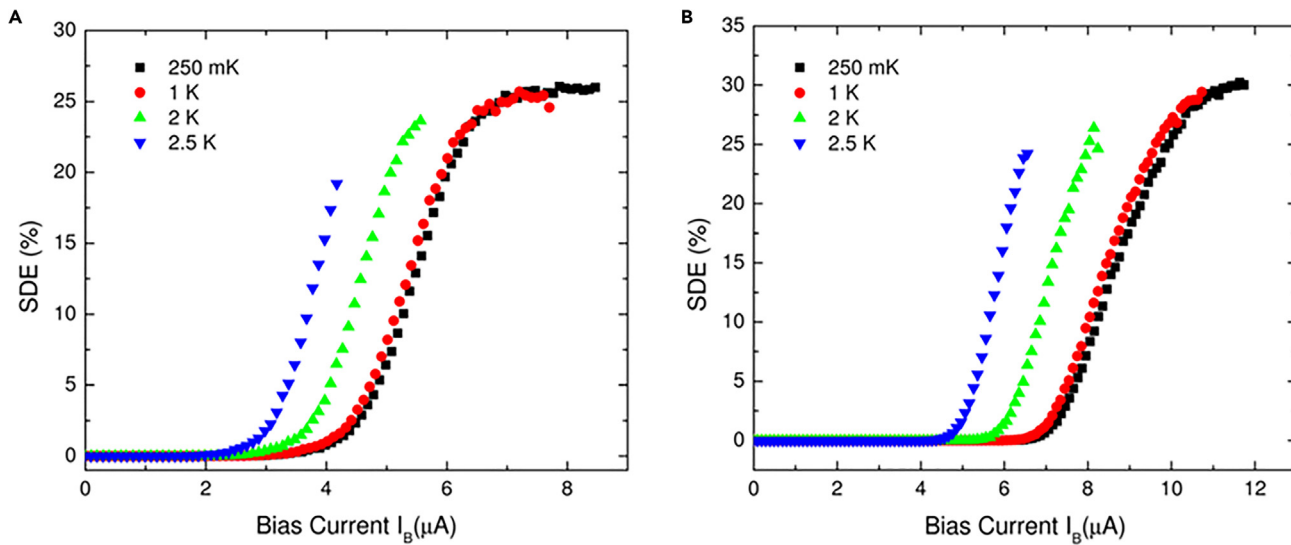


**Figure 5. System detection efficiency vs. bias current for MoGe-based SNSPDs with varying width and temperatures**

System detection efficiency vs. bias current for MoGe-based SNSPDs with width (A) 110 nm and (B) 150 nm performed at different temperatures 250 mK, 1 K, 2 K, 2.5 K, Reproduced with permission,<sup>131</sup> Copyright 2014, Applied Physics Letters.

signal-to-noise ratio and high switching current led to improved timing jitter for MoGe SNSPDs in comparison to WSi detectors. All these properties established MoGe-based detectors useful for applications requiring operation in a close-cycle cryocooler at 2.5 K.

### MgB<sub>2</sub>

Day and Nagamatsu in 2001<sup>145,146</sup> reported superconductivity in a new class of inexpensive, simple, and high performance superconductor, MgB<sub>2</sub>. A T<sub>C</sub> of ~39 K reported for MgB<sub>2</sub> was the record high for a non-oxide compound. In the years to follow, attention was paid to the growth of MgB<sub>2</sub> films for different applications.<sup>147–149</sup> The unique properties, such as a superconducting energy gap similar to NbN, high T<sub>C</sub>, adequate anisotropy, and transparency of grain boundaries qualifies it to be used for the fabrication of superconducting devices. In early 2007, Monticone et al.<sup>150</sup> fabricated 250–500 nm wide MgB<sub>2</sub> meander lines using the e-beam lithography technique. They reported a critical current density of 8 MA/cm<sup>2</sup> at 9.5 K for meander lines of 270 nm width. The strong phonon-electron coupling in MgB<sub>2</sub> along with the high phonon frequency observed in boron bond-stretching mode gave rise to smaller electron-phonon relaxation time and phonon escape time, indicating faster response, as compared to NbN-based detectors.<sup>151</sup> Khafizov et al.<sup>152</sup> intended to understand the underlying photon response mechanism in current-biased MgB<sub>2</sub> micro-bridges by performing time-resolved photo impedance measurements. They observed a picosecond kinetic photo-response indicating the possibility of using MgB<sub>2</sub> bridges as potential candidates for efficient and fast photon detection. Different groups<sup>153,154</sup> fabricated 10-nm thick MgB<sub>2</sub> thin films with T<sub>C</sub> ~21 K, using molecular-beam epitaxy, and studied its photo-detection properties.

Shibata et al.<sup>155</sup> studied the optical response of MgB<sub>2</sub>-based detectors. A lift-off technique using a Si/C mask was employed to fabricate 100–150 nm wide, 10 nm thick MgB<sub>2</sub> nanowires. While a 150 nm wide nanowire showed the capability of detecting a single photon at 405 nm wavelength but ceased to detect a 1560 nm photon, the nanowire having 100 nm width could detect photons in the range of 405–1560 nm. In various studies, 5 nm thick MgB<sub>2</sub> films, having T<sub>C</sub> > 30 K, have been deposited using a hybrid physical chemical vapor deposition technique (HPCVD).<sup>151,156,157</sup> Charaev et al. recently reported a response time of ns range with observance of single-photon detection (up to 20 K temperature) in 100 μm long, 1–5 μm wide, and 12 nm thick MgB<sub>2</sub> microwires at 1.55 μm optical wavelength.<sup>158</sup> Thus, MgB<sub>2</sub> can possibly be employed as a high-performance SNSPD.

### Oxide-based superconductors

Enomoto et al. fabricated the first oxide-based superconducting detector in a 150 nm thick microwire constriction of BaPb<sub>0.7</sub>Bi<sub>0.3</sub>O<sub>3</sub>-based Josephson junction. The peak responsivity at 1–8 μm range gave a basic idea of the preferable light range for the detectors.<sup>159</sup> Yoshisato et al. fabricated micro lines from granular YBCO thick films, which functioned as Josephson junctions along the grain boundaries of particles and showed excellent response to microwave radiations.<sup>160</sup> Leung et al. observed a bolometric response in 1 μm thick YBCO granular film deposited over the sapphire substrate.<sup>161</sup> The YBCO patterns of 50–200 μm length, 10–100 μm width, and 40 nm thickness deposited over MgO substrate exhibited bolometric and non-bolometric responses in nano and pico seconds range, for T ~ T<sub>C</sub> and T ≪ T<sub>C</sub>, respectively, as reported by Freknel et al. They used a laser source of 630–1060 nm range to illuminate the devices.<sup>162</sup> Carr et al. observed a fast bolometric response in YBCO thin films of 50–500 μm width and 40–320 nm thickness deposited over sapphire and MgO substrates.<sup>163</sup> Zheng et al. observed a bolometric R-T behavior with few non-linear regions in 150 nm thick YBCO thin films of 200 × 10 μm<sup>2</sup> cross-section area when

illuminated with 10.6 nm CO<sub>2</sub> Laser source.<sup>164</sup> Eidelloth reported slow and fast responses, with higher and lower responsivity, respectively, in 200 nm thick YBCO thin films.<sup>165</sup> The response dynamics were affected by crystallinity, bias current, operating temperature, and Laser frequency in all the above studies. Eidelloth and Frank observed an inverse dependence of wavelength on the responsivity for 0.8–80 μm thick bridges of Bi-Sr-Ca-Cu-O thin films of 1.5 × 1 mm<sup>2</sup> cross-section area when shined with visible photons.<sup>166</sup> Schneider et al. observed photo-response in Tl-Ba-Ca-Cu-O patterns of 10 mm × 10 mm × 1 μm dimensions with the maximum responsivity of 10 V/W when shined with a CO<sub>2</sub> Laser of 10–500 μm wavelength. A faster response with sharper peak for lower energy photons ( $\lambda > 66 \mu\text{m}$ ) and vice-versa was observed. Also, the faster response observed at  $T \ll T_C$  slowed down with temperature approaching the  $T_C$ .<sup>167</sup> In all the above photon detection events, a significant role of grain boundaries leading to faster responses along inter-granular phase slips was observed. The non-bolometric signals from granular superconducting thin films were attributed to the Josephson effect, which led to phase slips along the grain boundaries.<sup>168,169</sup> In some way, the experimental observations in cuprate oxides encouraged studying the phase slips and other associated physics that lead to faster responses in the later designed oxide-based detectors.

In oxide-based superconductors, charge transfer along adjacent CuO<sub>2</sub> planes is responsible for superconductivity, which is supported by the fact that rise in  $T_C$  with increasing CuO<sub>2</sub> layers in some families. There have been more than 200 high  $T_C$  superconductors (HTS) discovered so far. We have discussed material properties and photo-response exhibited by a few HTS materials.

### LSCO

Litombe et al. fabricated 80 nm wide La<sub>2-x</sub>Sr<sub>x</sub>CuO<sub>4</sub>/LaSrAlO<sub>4</sub> wires by e-beam lithography and Ar<sup>+</sup> ion milling. They emphasized optimum milling parameters for the retainment of good superconducting properties. The  $T_C$  of 41 K and a  $J_C$  of 10<sup>8</sup> A/cm<sup>2</sup> were reported in 200 nm wide and 26.4 nm thick LSCO wires.<sup>52</sup> Figure 6A shows a patterned LSCO wire to pass current and measuring of voltage across the nanowires. The critical current density against applied voltage as a function of wire width is shown in Figure 6B. Shibata et al. studied photo-response in 10 μm long, 100 nm wide, and 5 nm thick La<sub>1.85</sub>Sr<sub>0.15</sub>CuO<sub>4</sub> films deposited over LaSrAlO<sub>4</sub> substrate. A  $T_C$  of 41.6 K with higher switching current values at lower temperatures and vice-versa explained the temperature-dependent resistive phase transitions (Figure 6C). The temperature of 30 K was reported to be the detection threshold.<sup>170</sup>

### Rare-earth cuprate oxides

The cuprate-based HTSs consist of an active block: (CuO<sub>2</sub>|R(CuO<sub>2</sub>)<sub>n-1</sub>, where R = rare earth or Y, n = 1, 2, ...) and a charge reservoir block: (EO(AO)<sub>m</sub> EO, where E = Ca, Sr, Ba, and so forth, A = Bi, Tl, Pb, Hg, Cu or rare earth element, and m = 0, 1, 2). The RBa<sub>2</sub>Cu<sub>3</sub>O<sub>6+δ</sub> (RBCO) where R represents rare earth elements such as; Nd, Gd, Sm, Er, Eu, Tm, Yb, Lu, and so forth<sup>174</sup> have shown  $T_C$  of 90–100 K. The  $T_C$  value varies as a function of temperature, pressure, and oxygen content during bulk synthesis as well as thin film depositions. A reduction in dimensionality is observed to affect the atomic arrangement and oxygen stoichiometry. Therefore, thin films of rare earth cuprates show lower  $T_C$  compared to their bulk form, possibly due to the modified band gap at reduced dimensions. These materials have shown a wide range of potential applications in fields of energy storage, power transmission, MRI, Josephson junction set-ups, and IR sensors, and so forth.<sup>175–177</sup>

**YBCO.** YBa<sub>2</sub>Cu<sub>3</sub>O<sub>6+δ</sub> has been explored the most for photon detection among the rare earth cuprates, possibly due to its easier way of synthesis with the proper stoichiometry of atoms maintained in bulk and thin film form. The YBa<sub>2</sub>Cu<sub>3</sub>O<sub>6+δ</sub> unit cell has a perovskite (ABO<sub>3</sub>) structure with two BaCuO<sub>3</sub> layers lying on both sides of the central YCuO<sub>3</sub> unit cell. The CuO chains in the orthogonal YBCO are distorted because of the possession of the initially vacant (1/2, 0, 0) site. The orthorhombic phase is defined by lattice parameters; a = 3.82 Å, b = 3.89 Å, and c = 11.68 Å along (100), (010), and (001) directions, respectively. An individual perovskite cell contains a Barium atom at the body center of the top and bottom unit-cell, Yttrium at the body center of the middle one, Copper atoms at the corners, and Oxygen atoms at the middle edge position. In YBCO crystal, the layers are stacked, along the c-axis, in the following sequence CuO-BaO-CuO<sub>2</sub>-Y-CuO<sub>2</sub>-BaO-CuO.<sup>178</sup> The parameters such as unit cell parameter, critical current density, and conductivity, and so forth have different values along the c-axis and ab-plane.

In YBa<sub>2</sub>Cu<sub>3</sub>O<sub>6+δ</sub>, the arrangement of oxygen atoms in the unit cell during target synthesis and thin film deposition leads to superconductivity for  $x = 6+\delta$ . It is an insulator at zero doping ( $\delta = 0$ ) with anti-ferromagnetic spin ordering and tetragonal crystal structure (for temperature of 700–900°C). A transition from tetragonal to superconducting orthorhombic phase takes place when the temperature is decreased with a simultaneous increase in the oxygen content. For  $p = 0.16$  (where p is the number of holes per copper atom), the maximum  $T_C$  of ~94 K is reported in bulk YBCO crystals. The superconductivity starts depleting for  $x > 7$  ( $p = 0.27$ ) (Figure 8A). Thus, in YBCO, the critical parameters are influenced by oxygen concentration.<sup>179,180</sup> It is essential to have optimized growth conditions in layered cuprates. Also, the low reflectivity (<10%) and low transmissivity (~20%) of YBCO thin films for 1–2.5 eV photons (visible region) point to the high absorption of radiations, which would lead to a good photo-response from these devices.<sup>181</sup>

Several groups have studied the photo-response in YBa<sub>2</sub>Cu<sub>3</sub>O<sub>7-x</sub>. Curtz et al. deposited 12 nm thick YBCO film over the STO surface by RF magnetron sputtering with gold and PBCO capping layer. The 50 μm wide YBCO bridge was fabricated by photolithography and FIB using Ga<sup>3+</sup> ion with 50 pA beam current. The dependence of resistivity on temperature and current density was studied in detail, and a  $J_C(0)$  value of 4.1 MA/cm<sup>2</sup> was reported.<sup>183</sup> Probst et al. have elaborated the photo-response from 15 to 50 nm thick micro bridges of YBCO deposited over sapphire (Al<sub>2</sub>O<sub>3</sub>) (back illumination provided for better photo-response). The  $T_C$  and  $J_C$  values were plotted for 2 μm × 4.5 μm wires, which exhibited a linear scaling with decreasing wire thickness. A clear I-V hysteresis loop was obtained for 30 nm thin films with distinct switching values for voltage and current. The optical measurements for 30 nm thick films represented a response of 600 mV amplitude to low energetic

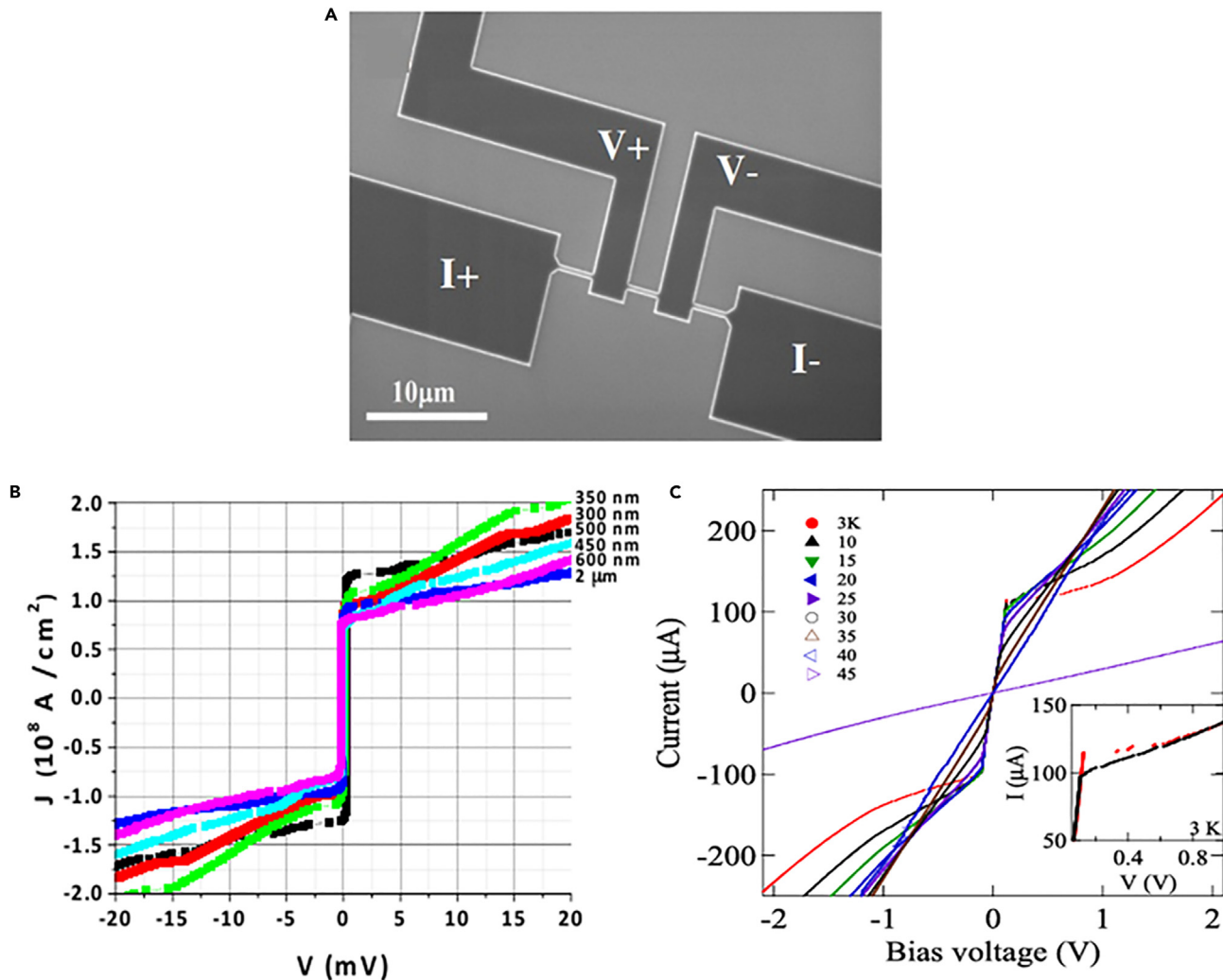


**Figure 6. LSCO nanowires**

(A) Patterned LSCO wire for the passing of I and measuring of V across the nanowires, (B) Critical current density against applied voltage, as a function of wire width.

(A and B) Reproduced with permission.<sup>52</sup> Copyright 2014, Elsevier.

(C) I-V curves as a function of different temperatures for LSCO nanowires; inset shows I-V at 3 K temperature. Reproduced with permissions.<sup>170</sup> Copyright 2017, IOP Publishing group.

THz radiations. In contrast, a 120 mV voltage was observed for comparatively high energetic optical pulses.<sup>184</sup> Nawaz et al. carried out transport measurements for a set of 200–3000 nm long, 40–200 nm wide, and 50 nm thick Au capped YBCO/MgO nanowires, patterned using e-beam lithography. The hysteretic I-V curves, along with  $J_C$  values as a function of wire-width were plotted for both capped and uncapped wires. A maximum  $J_C$  of  $10^8$  A/cm<sup>2</sup> was reported for 95 nm wide capped wire, exhibiting Josephson-like steps in I-V curves, which were attributed to phase slips in the ultra-narrow wires.<sup>185</sup> The same group studied voltage signals as a function of temperature and bias current for 40 nm × 90 nm × 50 nm YBCO/LAO wires. The critical current scaling with temperature i.e.,  $I_C = I_0 [1 - (\frac{T}{T_C})^2]^{3/2}$  (as per G-L equations) was observed, and a  $J_{C\ max}$  of 20 MA/cm<sup>2</sup> was reported.<sup>55</sup> Amari et al. fabricated 450 μm long nanowires of three different widths (100, 200, and 750 nm) and 30 nm thickness from YBCO thin films by Ar<sup>+</sup> ion etching, e-beam lithography, and oxygen plasma etching. There were observed higher switching values of current-voltage for lower temperatures, and vice-versa. The  $I_C$ -T scaling equation fitted well with the experimental data with a  $J_{C\ max} = 4.3$  MA/cm<sup>2</sup> for 100 nm wide wire. The inductance (L) and normalized resistance ( $R_N$ ) decreased with the increasing wire width for varying temperatures, which provided an idea of photo response dynamics.<sup>186</sup>

Arpaia et al. studied photo response to X-rays by 20–150 nm thick YBCO-based detectors. The nature of I-V hysteresis curves was studied in detail as a function of temperature. There were observed wider loops with sharper switching values for lower temperatures, and the  $J_C$  – T scaling law followed the G-L equations as derived for thin films.<sup>187</sup> Ejrnaes et al. observed hysteretic I-V loops for 80 nm long, 65 nm

wide, and 10 nm thick YBCO/MgO nano strips. The wires with  $J_C$  beyond 5 MA/cm<sup>2</sup> showed sharp switching voltage, whereas, flux flow such as behavior was noted for  $J_C$  below 5 MA/cm<sup>2</sup>. The hysteretic I-V curves up to 9.3 K were analyzed, and the highest  $J_C$  value of 34 MA/cm<sup>2</sup> was reported. It was a crucial achievement in the direction of single photon sensitivity.<sup>188</sup> The phase slip signals in 2 μm × 300 nm × 8.2 nm YBCO/STO nanowires were studied by Lyatti et al. They studied the switching and re-trapping currents for different widths of nanowires and operating temperatures. The higher LED irradiance shifted the switching current to a lower value, and vice-versa. Moreover, the photon-induced switching or hotspot formation was studied as single photon events considering the decay time constants involved. This was another crucial development toward approaching single photon counts in high  $T_C$  cuprate oxides.<sup>189</sup> Kumar et al. observed ultrafast response, consisting of 850 ps rise time, 1250 ps day time, and 100 ps timing jitter in  $\text{YBa}_2\text{Cu}_3\text{O}_{7-x}$ -based microwires at 76 K temperature.<sup>190</sup> Amari et al. studied I-V characteristics in 30 nm thick  $\text{YBa}_2\text{Cu}_3\text{O}_{7-x}$  nanowires of 0.5–500 μm × 0.1–5 μm cross-section, capped with CeO<sub>2</sub> and Au and patterned by Laser beam lithography. A sharp resistive transition occurred for temperatures above 85 K and hysteretic I-V curves ( $J_C$  maximum of 10 MA/cm<sup>2</sup>) with broader loop area were observed for decreasing operating temperatures.<sup>191</sup>

**BSCCO.** The  $\text{Bi}_2\text{Sr}_2\text{Ca}_2\text{Cu}_3\text{O}_{10}$  (B2223) coated wires were first used for current transport and superconducting maglev trains. The  $T_C$  and c-axis length increases with increasing n-value from 1 to 3, which confirms the role of interlayer coupling among CuO<sub>2</sub> layers.<sup>192</sup> The brittleness of these materials along their plane of unit cell repetition has hindered their exploration for device applications for a long time.

Seifert et al. in 2021, fabricated 15 nm thick  $\text{Bi}_2\text{Sr}_2\text{CaCu}_2\text{O}_8$  thin films by mechanical exfoliation from bulk BSCCO crystal. The film was transferred onto the SiO<sub>2</sub> substrate followed by coupling with a silicon nitride (SiN) waveguide and capped with hexagonal boron nitride (hBN). A  $T_C$  of 91 K for 100 nm wide patterns fabricated by He<sup>+</sup> FIB was noted. The I-V curves exhibited hysteretic behavior at the 15–30 K temperature range, required for self-stabilized hotspot formation in nanowires (Figure 7D). The nano-bridges responded to 1550 nm long radiations with a fast rise time of 220 ps followed by a slow decay time of 2 ns. The responsivity (ratio of the output voltage to Laser power) showed its maximum and minimum values at 15 K and 77 K, respectively. Thus, an easier fabrication, higher  $T_C$ , and ultrafast detection provided BSCCO a unique position in the family of cuprate-based detectors.<sup>173</sup> Ghosh et al. comparatively studied I-V characteristics and photo-response in BSCCO in the visible range for 30 μm × 700 nm × 9 nm nanowires and 3 μm × 300 nm × 12 nm nanowires. It was concluded that the responsivity of the detector can be improved by increasing the length and reducing the width and thickness of the superconducting nanowires.<sup>193</sup> Merino et al. recently reported a single photon response in 2.5 μm × 250 nm cross-sectional BSCCO nanopatterns deposited over SiO<sub>2</sub> and capped with hBN. The distinct hysteretic I-V curves were observed up to 30 K temperature for 1550 nm wavelength photons placing BSCCO as the first among high  $T_C$  superconductors to provide single photon detection (Figures 7A and 7B).<sup>171</sup> Charaev et al. also fabricated 56 μm × 100 nm cross-sectional BSCCO nanopatterns of 10–15 nm thickness over SiO<sub>2</sub> substrate and capped with hBN (Figure 7C). The devices showed single photon response up to 25 K with distinct hysteretic I-V curves for 1550 nm light.<sup>172</sup>

### Electron doped cuprates

The electron-doped cuprates have faster photo-response compared to hole-doped cuprates, hence they have attracted scientific interest over the past few years.<sup>182,194</sup> The partial substitution of cerium (Ce) into  $\text{RCuO}_4$  (R = La, Nd, Pr, and so forth) gives rise to this class of superconductors.<sup>195</sup> The electron and hole doped superconductors can be distinguished from the difference in their crystal structure and p-T phase diagram (Figure 8B).

Long et al. studied photo-response in 100 nm wide, 200 nm thick wires of  $\text{La}_{2-x}\text{Ce}_x\text{CuO}_4$  deposited over STO with  $T_C$  of 26 K for  $x = 0.11$ , which exhibited faster optical reflectivity to 790 nm long Ti: sapphire Laser beams, and the response was more rapid at lower temperature.<sup>196</sup> As reported by Charpentier et al., the 250 nm long, 150 nm wide, and 75 nm thick nanowires of  $\text{Pr}_{1.85}\text{Ce}_{0.15}\text{CuO}_4$  (PCCO) fabricated over  $(\text{LAO})_{0.3}\text{-Sr}_2\text{TaAlO}_6$  substrate showed  $T_C$  of 17 K. The observation of hysteretic I-V curves at the 3–17 K range established PCCO as a suitable material for photon detection.<sup>197</sup> The pump-probe experiments showing faster response dynamics in  $\text{Nd}_{2-x}\text{Ce}_x\text{CuO}_4$  films conducted by Avella et al.<sup>198</sup> encouraged Romano et al.<sup>194</sup> to fabricate sub-micron wires by photolithography to carry out photon detection measurements. The lack of ample work on electron doped cuprates in SNSPD gives a scope to study these materials and associated challenges for the same. Ejrinaes et al. fabricated microwire photo-detectors of 12.5 μm × 3 μm cross-sectional area of  $\text{Nb}_{0.15}\text{Re}_{0.85}$ , where they observed single photon response to 1.5 μm wavelength at an operating temperature below 2 K, along with the maximum current density of 0.26 MA/cm<sup>2</sup>.<sup>199</sup>

### F/S heterostructure for functional capping

Few oxide capping layers with similar unit cell crystallography were grown over the oxide ultrathin films, which provided protection against contamination, moisture, and CO<sub>2</sub> and influenced the  $T_C$ , mainly by facilitating charge transfer along CuO<sub>2</sub> planes through the interface. The Au capping layer is commonly used to preserve and influence the electro-optical properties of superconducting thin films. However, Au cannot be used for SNSPD device fabrication, due to its high reflectivity and high electrical conductivity. The ferromagnetic capping, especially  $\text{La}_{0.7}\text{Sr}_{0.3}\text{MnO}_3$  (LSMO) and  $\text{La}_{0.7}\text{Ca}_{0.3}\text{MnO}_3$  (LCMO), being structurally compatible with YBCO crystal structure, can provide favorable outcomes in the direction of photon detection.<sup>200,201</sup> As reported by Arpaia et al.,<sup>187</sup> the LSMO/YBCO exhibited enhanced  $T_C$  and faster relaxation time compared to YBCO or Au/YBCO. The post-annealing in the presence of oxygen (O<sub>2</sub>) or ozone (O<sub>3</sub>) restored the oxygen stoichiometry.<sup>202</sup> The interfaces with spin diffusion length ( $2\xi_F$ ) of ≈ 10 nm along LSMO/YBCO/LSMO multilayer provided a bound state to study and exploit interface effects.<sup>203</sup>

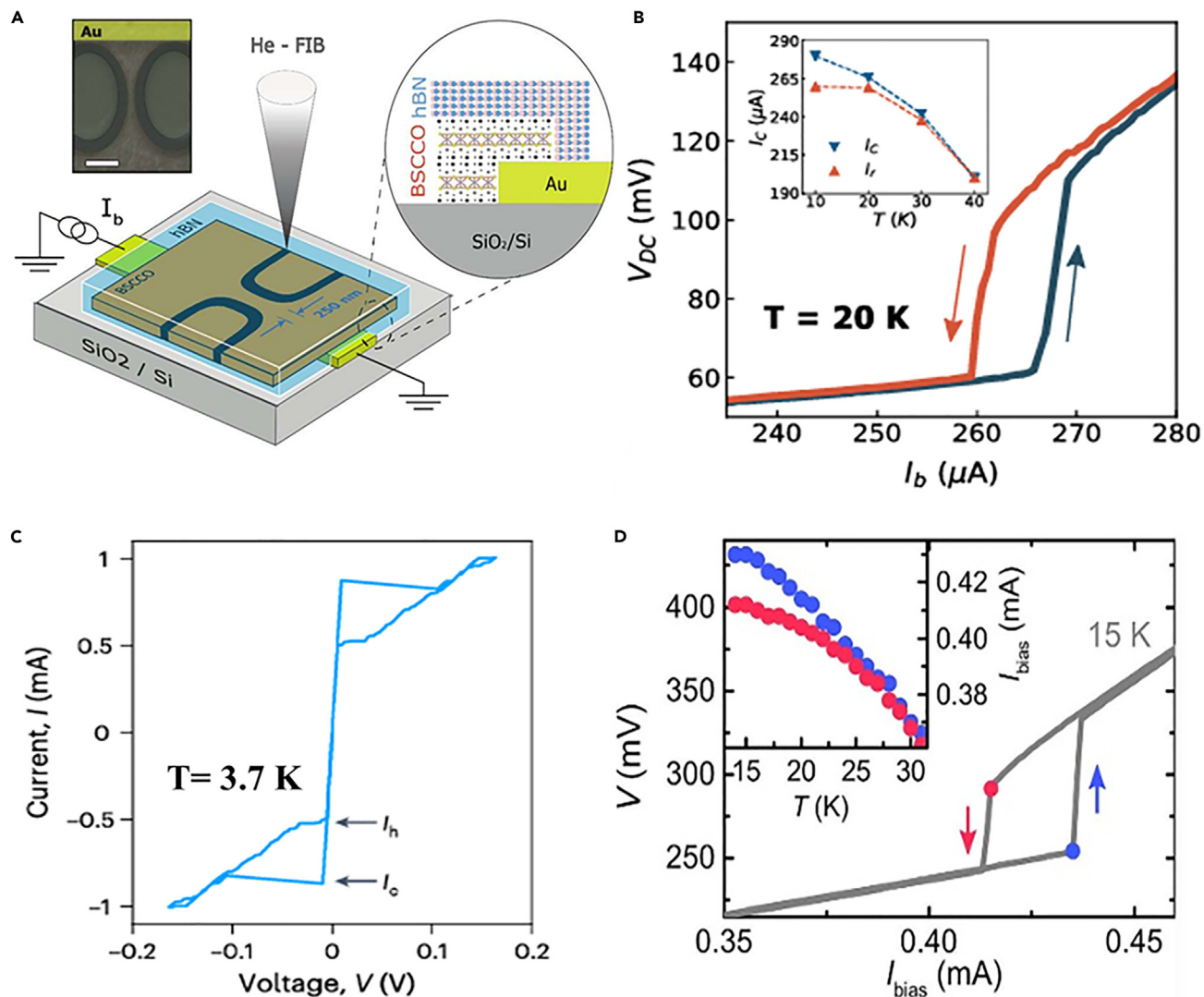


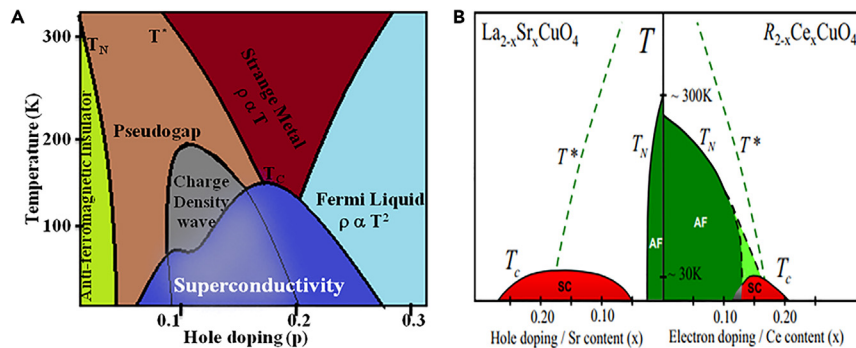
**Figure 7. BSCCO nanowires for photodetection**

(A) BSCCO nanowire, capped with hBN and patterned by He<sup>+</sup> ion beam, (B) I-V characteristic curve for 250 nm thick BSCCO nanowire at 20 K temperature (inset shows temperature dependent critical current (blue) and re-trapping current (red) values), Reproduced with permission,<sup>171</sup> Copyright 2023, IOP publishing group. (C) I-V characteristic curve for 100 nm wide, 10–15 nm thick BSCCO nanopattern at 3.7 K temperature, Reproduced with permission,<sup>172</sup> Copyright 2024, Springer Nature Ltd (D) I-V characteristic curve for 100 nm wide, 15 nm thick BSCCO nanowire (inset shows temperature dependent critical current (blue) and re-trapping current (red) values), Reproduced with permission,<sup>173</sup> Copyright 2021, IOP Publishing group.

Arpaia et al. deposited 15 nm thin film of La<sub>0.7</sub>Sr<sub>0.3</sub>MnO<sub>3</sub> over 50 nm thick YBa<sub>2</sub>Cu<sub>3</sub>O<sub>7-x</sub> film. It helped to retain the uniformity of thin films during patterning, and the  $T_C$  was enhanced by around 2 K. The rise in  $T_C$  was attributed to a fall in resistance due to the parallel combination of  $R_{YBCO}$  and  $R_{LSMO}$ . The photo-response of YBCO/LSMO exhibited voltage amplitude twice as that of bare YBCO films, as shown in Figure 9A. Pepe et al. observed a faster photo-response to Laser radiations for YBCO/LSMO bilayers, compared to YBCO monolayer, in terms of reflectivity change with respect to delay time in pump-probe measurements,<sup>204</sup> as shown in Figure 9B. Some other studies found reduced dark counts for YBCO/LSMO nanowires, as compared to those found for YBCO nanowires. As shown in Figures 9C and 9D, the optical responses from YBCO and YBCO/LSMO nanowires (insets compare I-V hysteresis loops at 5 K temperature) indicated distinct and broader I-V curves for the bilayers.<sup>205</sup> Moreover, a good quality capping layer over oxide thin films is required before patterning to obtain SNSPD devices with superior photon sensing capability.

### Underdoped high $T_C$ superconductor cuprate nanowires

The formation of charge density wave (CDW) in the underdoped cuprate oxide superconductors creates a different order parameter, named correlation length (larger than coherence length ( $\xi$ ) of optimally doped materials). The CDW periodically opposes the change in resistance

**Figure 8. Hole doped and electron doped cuprates**

(A) Phase diagram of  $\text{YBa}_2\text{Cu}_3\text{O}_{7-\chi}$  showing various short orders arising as a function of hole doping and temperature, (B) Comparative phase diagram for electron and hole doped cuprates. Reproduced with permission.<sup>182</sup> Copyright 2010, American Physical Society.

due to varying electric or magnetic fields (oscillating magneto-resistance).<sup>207,208</sup> A rise in the first upper critical field ( $H_{C1}$ ) with a lesser  $T_C$  has been found for the underdoped HTS.<sup>209</sup> Another study carried out by Ramshaw et al. for measuring  $H_C$  with varying oxygen doping confirmed a higher value of critical field ( $H_{C2}$ ) at the underdoped state ( $p < 0.11$ ) with the minimum  $H_{C2}$  at  $p = 0.11$ .<sup>210</sup> The reduction in oxygen concentration in ultrathin HTS films increases the resistivity due to the reduced number of charge carriers and reduced coupling among adjacent  $\text{CuO}_2$  layers. However, this concept worked in favor of SNSPDs. Andersson et al. fabricated underdoped YBCO nanowires with 50 nm thickness and 100–600 nm width over  $\text{LaAlO}_3$  and obtained broader hysteretic I-V curves, as compared to 15 nm thick optimally doped wires with other parameters similar (Figure 10).<sup>211</sup>

Thus, a higher resistivity and higher switching value for I-V curves of underdoped nanowires favored their implementation toward SNSPD realization.

## DISCUSSION ON DIFFERENT CRITICAL PARAMETERS

The superconducting critical parameters (temperature, magnetic field, and current density) exhibit parabolic interdependency on each other. However, the nature of curves and their upper critical values get modified with dimensions. The magnetic field shows a quadratic dependence on temperature, i.e.,  $H_C(T) = H_C(0)[1 - (\frac{T}{T_C})^2]$ ,<sup>212</sup> whereas, the current density is dependent on temperature as follows;  $J_C = J_0[1 - (\frac{T}{T_C})]^n$ ; where  $n$  value depends on dimension and crystallinity of the thin film.<sup>213</sup> It is experimentally confirmed that  $n = 3/2$  for cuprate thin films deposited over different substrates.<sup>214</sup> Therefore, a low working temperature essentially helps to achieve higher values of  $H_C$  and  $J_C$ , preferred for better superconducting properties.

The critical current sets an upper limit on biasing current that has to be passed through a uniform wire. It is essential to achieve a higher  $J_C$  for desired SNSPD properties. An ultrahigh  $J_C$  of  $1.3 \times 10^9 \text{ A/cm}^2$  was reported by Jiang et al. for YBCO nano-bridges joining two bulk superconductors.<sup>47</sup> A high  $J_C$  of  $10^8 \text{ A/cm}^2$  at 4.2 K was reported by Nawaz et al. for Au capped  $200 \times 50 \times 50 \text{ nm}^3$  YBCO/MgO(110).<sup>185</sup> A  $J_C$  value of  $10^7 \text{ A/cm}^2$  was reported by Borsoi for Au/Ti capped YBCO/CeO<sub>2</sub>/YSZ.<sup>215</sup> More importantly, the hysteretic I-V curves for  $J_C > 5 \times 10^6 \text{ A/cm}^2$ , reported for YBCO ultrathin films emphasized switching taking place due to high current density rather than grain boundaries material and geometry.<sup>216</sup> It is required to have patterned wires with higher  $J_C$  values for SNSPD devices. The voids, lattice defects, twin domains, and grain boundaries on the film and substrate surface act as pinning centers for the magnetic field and retain the higher critical current. Hence, a sufficient number of pinning centers along the surface can maintain a higher critical current. The pinning centers are artificially injected into thin films in the form of 0D (vacancies), 1D (columns), 2D (planar defects), and 3D (flux tube or doping of nano-particles) defects. These have notably enhanced the value of  $J_C$ .<sup>217</sup> There have been enhancements noticed in the in-field  $J_C$  through the substitution of atoms of other elements such as Nd, Gd, Sm, Eu, Dy, Tb, Pr, La and so forth into the Y site of YBCO by specific concentrations, attributed to induced strain effect on the  $\text{CuO}_2$  planes by doped atoms.<sup>218</sup> The BZO nano-rods doped into YBCO thin films acted as 1D defects, and enhanced the  $J_C$  and irreversible magnetic field.<sup>219</sup> A significant rise in  $T_C$  from 7 K to >100 K was observed by the doping of a certain amount of calcium ions into the Bi-Sr-Cu-O system.<sup>220</sup> However, no report exists on adopting pinning centers for SNSPD devices, the reason being, that pinning centers can affect the superconducting properties of HTSs, due to their shorter coherence length as compared to the distance between adjacent flux tubes.<sup>212</sup>

## TWO TEMPERATURE (2T) MODEL

Semenov et al.<sup>39</sup> explained the two temperature models by using the concept of different values of temperatures, i.e.,  $T_e$  and  $T_p$  for electron and phonon sub-systems, respectively, to understand the non-equilibrium photo-response in HTSs. The idea was to simplify the understanding of photo-response in three steps,<sup>221</sup> i.e.,

- (a) breaking of cooper pairs into quasi-particles
- (b) heat exchange between electrons and phonons

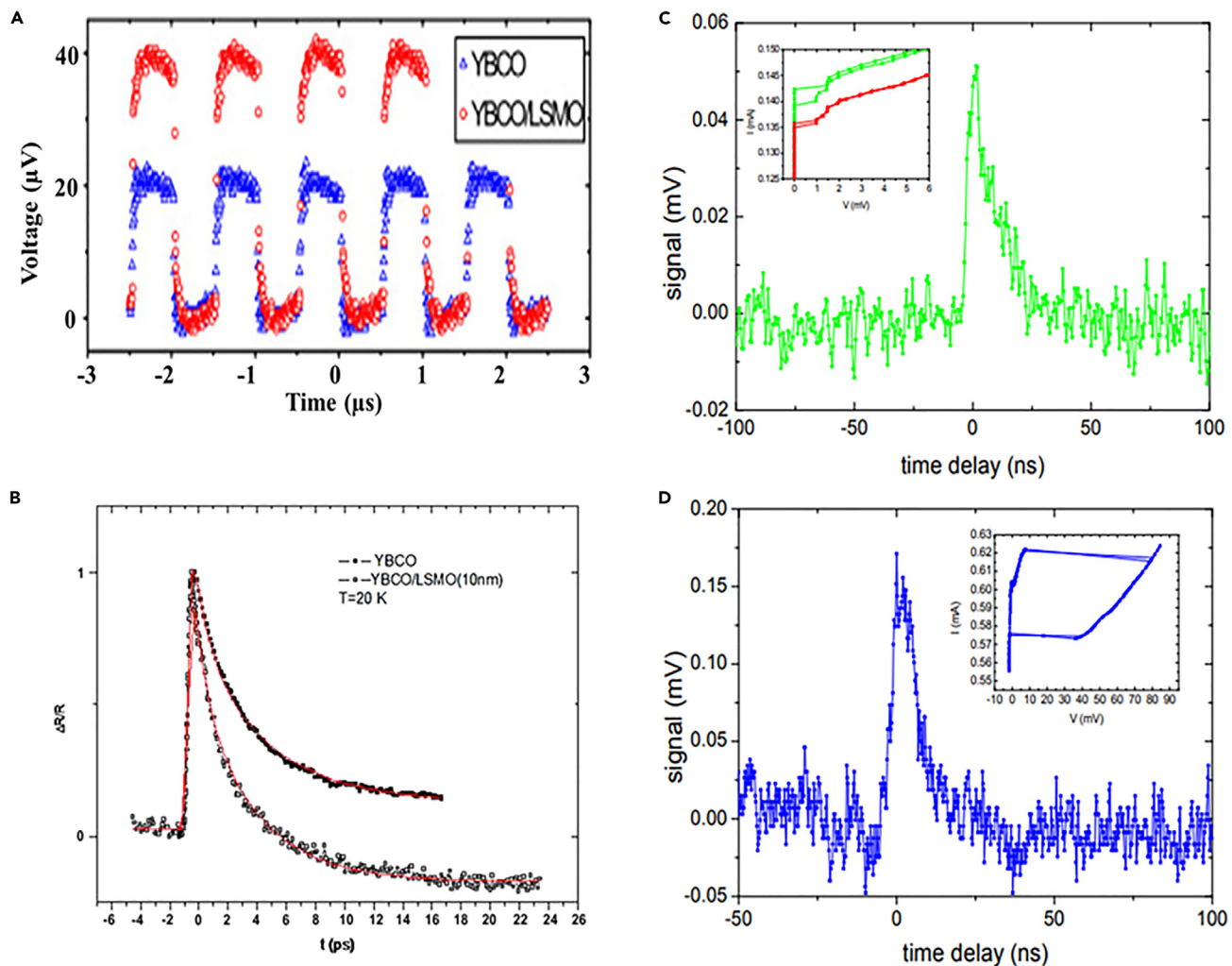


**Figure 9. Comparison of photo response curves for YBCO nanowires with and without ferromagnetic capping layers**

(A) Comparison of voltage output amplitude of YBCO and YBCO/LSMO nanowires. Reproduced with permission,<sup>206</sup> Copyright 2014, IOP Publishing Ltd.  
(B) Comparison of reflectivity to LASER signal with time for YBCO and YBCO/LSMO. Reproduced with permission,<sup>204</sup> Copyright 2009, Elsevier.

(C) Output signal with respect to delay time for YBCO and (D) YBCO/LSMO nanowires, respectively (insets show I-V hysteresis loops at 5 K temperature). Reproduced with permission,<sup>205</sup> Copyright 2017, SPIE Proceedings.

(c) heat flow from the phonon system to the substrate

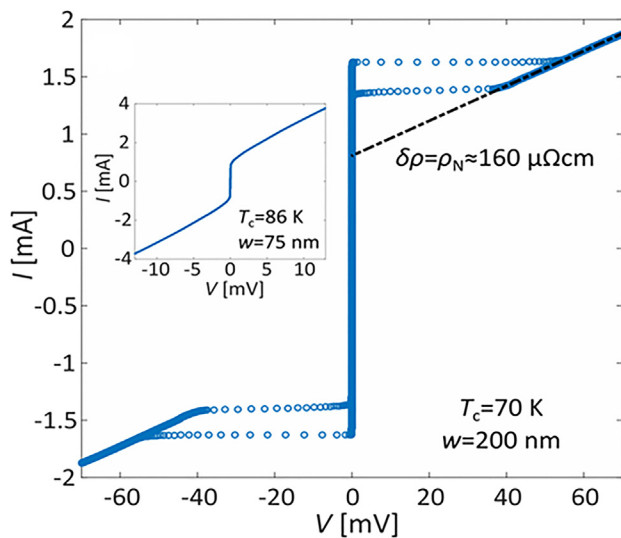
The heat distribution among electron, phonon, and substrate systems is schematically represented in Figure 11. The time constants are;  $\tau_{e-e}$  (rise time due to heat absorption by electron system),  $\tau_{e-p}$  (decay time by heat dissipation from electron system to phonons), and  $\tau_{p-s}$  (decay time by heat dissipation from phonons to substrates). They were obtained by fitting the specific heat constants for electron and phonon systems ( $c_e$ ,  $c_p$ , respectively), power absorbed into the film ( $P(t)$ ), and the temperature changes ( $dT_e$ ,  $dT_p$ ) for electron, phonon into the heat balance equations.<sup>222</sup>

$$c_e \frac{dT_e}{dt} = \frac{\alpha P(t)}{V} - \frac{C_e}{\tau_{e-p}} (\tau_e - \tau_p)$$

$$c_p \frac{dT_p}{dt} = \frac{C_p}{\tau_{p-e}} (\tau_e - \tau_p) - \frac{C_p}{\tau_{p-s}} (\tau_p - \tau_s)$$

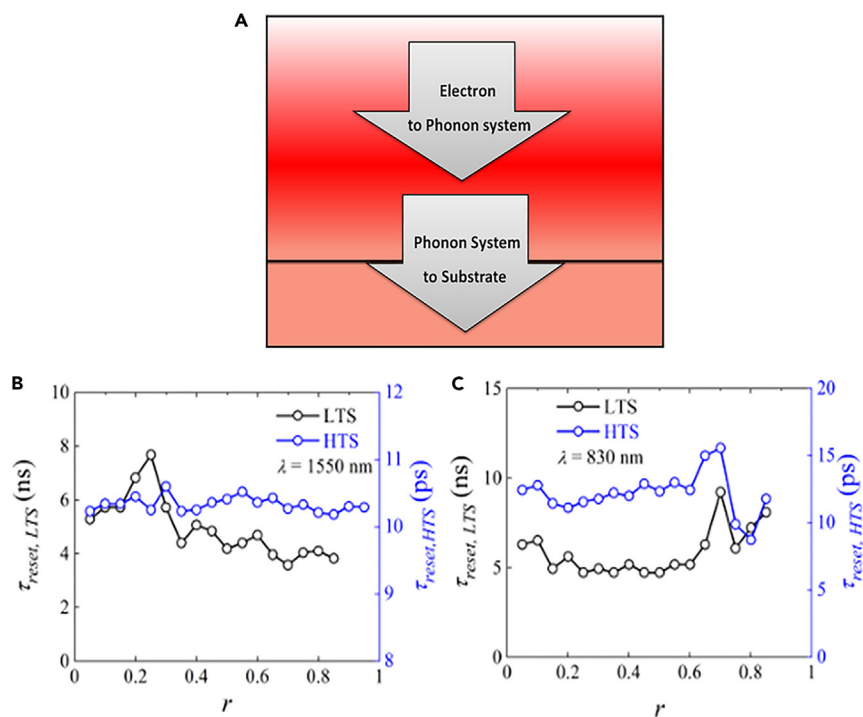
$\alpha$  = coefficient of absorption of radiation,  $V$  = volume of specimen.

The calculated values of time constants were comparable to the observed values. In HTS cuprates, the electronic system takes an active part in quasi-particles and photo response, whereas, the phonon system remains in thermal equilibrium. It was confirmed from the following

**Figure 10. I-V curves of YBCO nanowires grown with decreasing thickness and decreasing oxygen doping**

The inset shows the schematic comparison of I-V curves for nanowires with lesser thickness and optimal oxygen doping. Reproduced with permission,<sup>202</sup> Copyright 2017, American Physical Society.

values;  $\tau_{e-e} = 0.56\text{ ps}$  and  $\tau_{e-p} = 1.1\text{ ps}$  for YBCO thin film micro-bridges.<sup>222</sup> The time constants for YBCO thin films were one order lower than those of NbN thin films, which pointed to a faster relaxation dynamic in the cuprates. The larger  $C_p/C_e$  value of 38 in YBCO, compared to that of 6.5 in NbN indicated a lesser rate of back-flow of heat from the phonon system to the electron system in cuprates.<sup>224</sup> Haldar et al. compared different parameters of the 2T model calculated for Nb and YBCO, and observed photo-response in YBCO three orders faster than in Nb.<sup>223</sup> Thus, the 2T model explains the nonequilibrium, ultrafast response in cuprate thin films.

**Figure 11. Heat conduction model in SNSPD systems**

(A) Schematic picture showing heat transfer among electron-phonon-substrate system, (B and C) reset time ( $\tau_{\text{reset}}$ ) as a function of ratios of bias current to critical current densities ( $r = J_B/J_C$ ) for Nb (LTS) and YBCO (HTS) Reproduced with permission.<sup>223</sup> Copyright 2019, IOP Publishing group.

**Table 1.** Inter-comparison of superconducting parameters of materials used for SNSPD applications

Materials	NbN	NbTiN	WSi	TaN	MoGe	MoSi	NbSi	MgB <sub>2</sub>	YBCO
Bulk T <sub>c</sub> (K)	16	17	5	5	7.4	7.5	3.1	39	93
T <sub>c</sub> (K) Thickness (nm)	8.6 (3 nm)	9.6 (4.5 nm)	3.7 (4.5 nm)	8.3 (5 nm)	4.4 (7.5 nm)	4.2 (4 nm)	2 (10 nm)	39 (350 nm)	85.5 (3unit cell)
Band gap 2Δ <sub>0</sub> (meV)	4.9	5.17	1.52	1.52	2.2	2.28	0.94	11.86	28.29
J <sub>C</sub> (MA/cm <sup>2</sup> ) Meas. Temp. (K)	2-4 (4.2K) (2.9 K)	8 (250 mK)	0.8 (4.2 K)	4 (250mK)	1.2 (1.7 K)	1.1-2.5 (300mK)	0.14 (3 K)	1.1 (3 K)	14.4 (78 K)

## SUMMARY AND CONCLUSION

In this review, we have focused on summarizing the working principle, fabrication, and overall applications of nanowire-based photon detectors made of both high and low T<sub>c</sub> superconducting materials. The SNSPD device performance depends on the optimization of its characteristic interdependent parameters (detection efficiency, count rate, dark count rate, jitter time, and reset time). An inter-comparison of the superconducting properties pertaining to materials that have been used toward SNSPD fabrication are listed in Table 1. Traditionally, NbN and NbTiN superconductors are employed for the fabrication of SNSPD, whereas, the high T<sub>c</sub> cuprates hold an adventitious position in terms of faster temporal response over conventional low T<sub>c</sub> materials. However, the fast or non-bolometric response hinders the photon resolution. The critical parameters (I-V, J<sub>C</sub>, T<sub>c</sub>) varying with operating conditions have been discussed. It is desirable to employ high T<sub>c</sub> superconductors

**Table 2.** Major works carried out with HTS superconductors toward SNSPD applications

Material	Patterning	Active area geometry	Outcomes	Reference
YBCO/CeO <sub>2</sub> /Al <sub>2</sub> O <sub>3</sub> (capping)	CE, ion milling	2 μm × 4.5 μm × 15–50 nm	distinct I-V curves for w = 30 nm, fast and slow responses as function of temperature and energy of the signal	Probst et al. <sup>184</sup>
YBCO/STO/PBCO (capping)	PL, CE, and FIB	15-450 μm × 0.5–20 μm × 12 nm	R-T as a function of wire width, V-J and ρ-J with varying T, J <sub>C</sub> as function of T/T <sub>c</sub> , J <sub>C</sub> = 4.1 MA/cm <sup>2</sup>	Bo et al. <sup>226</sup>
YBCO/MgO/ Au (capping)	EBL, Ar <sup>+</sup> etching	200-3000 nm × 40–200 nm × 50 nm	Hysteretic I-V, sharp R-T with Au capping, J <sub>C max</sub> = 100 MA/cm <sup>2</sup> for w = 95 nm	Mori et al. <sup>211</sup>
LSCO/LSAO	MBE, EBL (λ = 1560 nm)	Nano-strips, 10 μm × 100 nm × 5 nm	Hysteretic I-V at 3 K, J <sub>C</sub> = 23MA/cm <sup>2</sup> , Photo-response up to 30 K temperature	Shibata et al. <sup>170</sup>
BSCCO/SiO <sub>2</sub>	He <sup>+</sup> FIB (λ = 1550 nm)	15 μm × 200 nm × 15 nm	Hysteretic I-V curve, fast and slow responses to optical signal as a function of temperature, GHz operation speed	Seifert et al. <sup>173</sup>
CeO <sub>2</sub> /YBCO/ Al <sub>2</sub> O <sub>3</sub>	IBE, EBL, Oxygen etching	100 μm × 100 nm × 30 nm	I-V as a function of T; R-T, and L-T as a function of wire width, inductance measured by resonant method, helpful in device performance	Lyatti et al. <sup>58</sup>
LSMO (15nm)/ YBCO (50nm)/LAO	by PLD, patterning: EBL, Ar <sup>+</sup> etching	10 μm × 100–300 nm × 50 nm	J <sub>C</sub> = 7.5 × 10 <sup>5</sup> A/cm <sup>2</sup> , the signal increased by twice as compared to YBCO following LSMO capping	Arpaia et al. <sup>206</sup>
Au (capping)/ YBCO/MgO/	EBL, Ar <sup>+</sup> etching	200 nm × 50–2000 nm × 10 nm	J <sub>C</sub> = 130 MA/cm <sup>2</sup> , Josephson-like steps in I-V curve for V = 10.3 GHz	Nawaz et al. <sup>185</sup>
YBCO/MgO	EBL, Ar <sup>+</sup> etching	80 nm × 65 nm × 10 nm	Hysteretic I-V curve, sharp voltage peaks for dark counts up to 9.3 K, J <sub>C</sub> = 34 MA/cm <sup>2</sup>	Ejrnaes et al. <sup>188</sup>
YBCO/STO	FIB	2 μm × 300 nm × 8.2 nm	I-V hysteretic curve, continuous switching and re-trapping current for illumination with visible radiation at 77 K temperature	Lyatti et al. <sup>189</sup>
hBN/BSCCO/SiO <sub>2</sub>	He <sup>+</sup> patterning	56 μm × 100 nm × 10–15 nm	hysteretic I-V curves, single photon response up to 25 K for 1550 nm light	Charaev et al. <sup>172</sup>
hBN/BSCCO/SiO <sub>2</sub>	He <sup>+</sup> patterning	2.5 μm × 250 nm	hysteretic I-V curves, single photon response up to 25 K for 1550 nm light	Merino et al. <sup>171</sup>

[PLD-Pulsed laser deposition, EBL-Electron beam lithography, PL-Photolithography, CE-Chemical etching, IBE-Ion beam etching, and FIB-Focussed ion beam].

for the fabrication of SNSPD so as to fully exploit their use.<sup>225</sup> We have discussed two significant advances for improved photon detection by the application of (i) ferromagnetic capping, and (ii) underdoped nanowires. In the approach toward realizing SNSPDs using two-dimensional high T<sub>C</sub> materials, single-photons have been detected in superconducting nanowires fabricated out of Bi<sub>2</sub>Sr<sub>2</sub>CaCu<sub>2</sub>O<sub>8+δ</sub> thin flakes of with single-photon response up to 25 K, which stands as a milestone in SNSPD. However, the inability to scale up the detector's active area is the limitation of exfoliated flakes. The major works in HTS oxide materials are summarized in Table 2.

This review led to the revelation of the following major points.

1. The material for SNSPD should have a low density of states and a low band gap, so as to allow incident photons to break a larger number of cooper pairs. The higher band gap ( $2\Delta$ ) in high T<sub>C</sub> cuprates (20–25 meV in YBCO compared to 1.5 meV in NbN) hinders them from photon number resolution.
2. A uniform geometry with a small cross-section area allows the hotspot to spread across the wire width. The difficulty in approaching high-quality ultrathin oxide wires with available patterning techniques prevents the utilization of these for SNSPDs.
3. The nonequilibrium heat distribution among electron and phonon systems in high T<sub>C</sub> cuprates, as stated in the 2T model prevents it from showing a bolometric response required for detectable signals.
4. An oxide-based HTS for single photon detection with optimized key parameters for practical applications is yet to be realized.

## ACKNOWLEDGMENTS

The authors are grateful to the Director, CSIR-NPL for state-of-the art facilities.

## AUTHOR CONTRIBUTIONS

ST: Conceptualization, data collection, formal analysis, writing of original draft, and review, and editing, KT: project administration, supervision, writing of original draft, review, and editing, and PP: methodology, writing, review, and editing.

## DECLARATION OF INTERESTS

The authors declare that they do not have any competing financial interests of personal relationships which could affect the work reported in this article.

## REFERENCES

1. Hadfield, R.H. (2009). Single-photon detectors for optical quantum information applications. *Nat. Photonics* 3, 696–705. <https://doi.org/10.1038/nphoton.2009.230>.
2. Natarajan, C.M., Tanner, M.G., and Hadfield, R.H. (2012). Superconducting nanowire single-photon detectors: physics and applications. *Supercond. Sci. Technol.* 25, 063001. <https://doi.org/10.1088/0953-2048/25/6/063001>.
3. Testardi, L.R. (1971). Destruction of superconductivity by laser light. *Phys. Rev. B* 4, 2189–2196. <https://doi.org/10.1103/PhysRevB.4.2189>.
4. Kraus, H. (1996). Superconductive bolometers and calorimeters. *Supercond. Sci. Technol.* 9, 827–842. <https://doi.org/10.1088/0953-2048/9/10/001>.
5. Gol'Tsman, G., Okunev, O., Chulkova, G., Lipatov, A., Semenov, A., Smirnov, K., Voronov, B., Dzardanov, A., Williams, C., and Sobolewski, R. (2001). Picosecond superconducting single-photon optical detector. *Appl. Phys. Lett.* 79, 705–707. <https://doi.org/10.1063/1.1388868>.
6. Guo, Q., Li, H., You, L., Zhang, W., Zhang, L., Wang, Z., Xie, X., and Qi, M. (2015). Single photon detector with high polarization sensitivity. *Sci. Rep.* 5, 9616. <https://doi.org/10.1038/srep09616>.
7. Xu, G.Z., Zhang, W.J., You, L.X., Xiong, J.M., Sun, X.Q., Huang, H., Ou, X., Pan, Y.M., Lv, C.L., Li, H., et al. (2021). Superconducting microstrip single-photon detector with system detection efficiency over 90% at 1550 nm. *Photon. Res.* 9, 958–967. <https://doi.org/10.1364/PRJ.419514>.
8. Shibata, H., Fukao, K., Kirigane, N., Karimoto, S., and Yamamoto, H. (2017). SNSPD with ultimate low system dark count rate using various cold filters. *IEEE Trans. Appl. Supercond.* 27, 1–4. <https://doi.org/10.1109/TASC.2016.2631947>.
9. Korzh, B., Zhao, Q.Y., Allmaras, J.P., Frasca, S., Autry, T.M., Bersin, E.A., Beyer, A.D., Briggs, R.M., Bumble, B., Colangelo, M., et al. (2020). Demonstration of sub-3 ps temporal resolution with a superconducting nanowire single-photon detector. *Nat. Photonics* 14, 250–255. <https://doi.org/10.1038/s41566-020-0589-x>.
10. Vetter, A., Ferrari, S., Rath, P., Alaei, R., Kahl, O., Kovalyuk, V., Diewald, S., Goltsman, G.N., Korneev, A., Rockstuhl, C., and Pernice, W.H.P. (2016). Cavity-enhanced and ultrafast superconducting single-photon detectors. *Nano Lett.* 16, 7085–7092. <https://doi.org/10.1021/acs.nanolett.6b03344>.
11. Koziy, A.A., Losev, A., Zavodilenko, V.V., Kurochkin, Y., and Gorbatsevich, A. (2021). Modern methods of detecting single photons and their application in quantum communications. *Quant. Electron.* 51, 655–669. <https://doi.org/10.1070/QEL17566>.
12. You, L. (2020). Superconducting nanowire single-photon detectors for quantum information. *Nanophotonics* 9, 2673–2692. <https://doi.org/10.1515/nanoph-2020-0186>.
13. Takesue, H., Dyer, S.D., Stevens, M.J., Verma, V., Mirin, R.P., and Nam, S.W. (2015). Quantum teleportation over 100 km of fiber using highly efficient superconducting nanowire single-photon detectors. *Optica* 2, 832–835. <https://doi.org/10.1364/OPTICA.2.000832>.
14. Guan, Y., Li, H., Li, X., Yin, R., Zhang, L., Wang, H., Zhu, G., Kang, L., Chen, J., and Wu, P. (2022). Lidar with superconducting nanowire single-photon detectors: Recent advances and developments. *Opt. Laser Eng.* 156, 107102. <https://doi.org/10.1016/j.optlaseng.2022.107102>.
15. Zhang, B., Guan, Y.-Q., Xia, L., Dong, D., Chen, Q., Xu, C., Wu, C., Huang, H., Zhang, L., Kang, L., et al. (2021). An all-day lidar for detecting soft targets over 100 km based on superconducting nanowire single-photon detectors. *Supercond. Sci. Technol.* 34, 034005. <https://doi.org/10.1088/1361-6668/ab576>.
16. O'Connor, E., Shearer, A., and O'Brien, K. (2019). Energy-sensitive detectors for astronomy: Past, present and future. *N. Astron. Rev.* 87, 101526. <https://doi.org/10.1016/j.newar.2020.101526>.
17. Bosco, G., Ke, D., Korzh, B., Boulliou, J., Lange, N., and Zbinden, H. (2016). Time-resolved singlet-oxygen luminescence detection with an efficient and practical semiconductor single-photon detector. *Biomed. Opt Express* 7, 211–224. <https://doi.org/10.1364/BOE.7.000211>.
18. Zhang, X., Wang, Q., and Schilling, A. (2016). Superconducting single X-ray photon detector based on W0.8Si02. *AIP Adv.* 6, 115104. <https://doi.org/10.1063/1.4967278>.
19. Yang, C., Si, M., Zhang, X., Yu, A., Huang, J., Pan, Y., Li, H., Li, L., Wang, Z., Zhang, S., et al. (2021). Large-area TaN superconducting microwire single photon detectors for X-ray detection. *Opt Express* 29, 21400–21408. <https://doi.org/10.1364/OE.422581>.
20. Gol'Tsman, G., Okunev, O., Chulkova, G., Lipatov, A., Dzardanov, A., Smirnov, K., Semenov, A., Voronov, B., Williams, C., and Sobolewski, R. (2001). Fabrication and properties of an ultrafast NbN hot-electron single-photon detector. *IEEE Trans. Appl. Phys.*

- Supercond. 11, 574–577. <https://doi.org/10.1109/77.919410>.
21. Yin, R., Wang, H., Zhang, L., Wang, X., Ma, L., Guan, Y., Yang, Z., Chen, Q., Tu, X., Zhao, Q., et al. (2023). Saturating quantum efficiency of SNSPDs with disorder manipulation of NbN films. *Supercond. Sci. Technol.* 36, 105016. <https://doi.org/10.1088/1361-6668/ac5f5aa>.
  22. Cheng, R., Wright, J., Xing, H.G., Jena, D., and Tang, H.X. (2020). Epitaxial niobium nitride superconducting nanowire single-photon detectors. *Appl. Phys. Lett.* 117, 132601. <https://doi.org/10.1063/5.0018818>.
  23. Ma, R., Shu, R., Zhang, X., Yu, A., Huang, J., Xiao, Y., Yu, H., Liu, X., Li, H., Eklund, P., et al. (2023). Single photon detection performance of highly disordered NbTiN thin films. *J. Phys. Commun.* 7, 055006. <https://doi.org/10.1088/2399-6528/acd747>.
  24. Qin, Z., Bao, H., Xu, T., Chen, S., Yang, S., Li, H., Wang, Z., Tu, X., Zhang, L., Zhao, Q., et al. (2024). Thermal-property optimization dominated by the stoichiometric ratio in W-Si superconducting single-photon detectors. *Phys. Rev. Appl.* 21, 024046. <https://doi.org/10.1103/PhysRevApplied.21.024046>.
  25. Nishikawa, M., Sawai, K., Sakai, K., Kirigane, N., Ohnishi, K., Nakano, W., Matsuo, Y., and Shibata, H. (2022). Fabrication of Superconducting Nanowire Single-Photon Detectors Using MoN. *IEEE Trans. Appl. Supercond.* 32, 1–4. <https://doi.org/10.1109/TASC.2022.3144967>.
  26. Zolotov, P., Semenov, A., Divochiy, A., and Goltzman, G. (2021). A comparison of VN and NbN thin films towards optimal SNSPD efficiency. *IEEE Trans. Appl. Supercond.* 31, 1–4. <https://doi.org/10.1109/TASC.2021.3059230>.
  27. Lita, A.E., Verma, V.B., Chiles, J., Mirin, R.P., and Nam, S.W. (2021). Mo  $\times$  Si1 – x: A versatile material for nanowire to microwire single-photon detectors from UV to near IR. *Supercond. Sci. Technol.* 34, 054001. <https://doi.org/10.1088/1361-6668/abeb00>.
  28. Liu, X., Xie, B., Sun, M., and Jiao, R. (2024). Multispectral MoSi superconducting nanowire single photon detector. *Opt. Commun.* 555, 130241. <https://doi.org/10.1016/j.optcom.2023.130241>.
  29. Polakovic, T., Armstrong, W., Karapetrov, G., Meziani, Z.-E., and Novosad, V. (2020). Unconventional applications of superconducting nanowire single photon detectors. *Nanomaterials* 10, 1198. <https://doi.org/10.3390/nano10061198>.
  30. Moody, G., and Islam, M.S. (2022). Materials for ultra-efficient, high-speed optoelectronics. *MRS Bull.* 47, 475–484. <https://doi.org/10.1557/s43577-022-00337-y>.
  31. Dauler, E.A., Grein, M.E., Kerman, A.J., Marsili, F., Miki, S., Nam, S.W., Shaw, M.D., Terai, H., Verma, V.B., and Yamashita, T. (2014). Review of superconducting nanowire single-photon detector system design options and demonstrated performance. *Opt. Eng.* 53, 081907. <https://doi.org/10.1117/1.OE.53.8.081907>.
  32. Yamashita, T., Miki, S., and Terai, H. (2017). Recent progress and application of superconducting nanowire single-photon detectors. *IEICE Trans. Electron. E100.C*, 274–282. <https://doi.org/10.1587/transle.E100.C.274>.
  33. Zadeh, E.I., Chang, J., Johannes, W.N.L., Gyger, S., Elshaari, A.W., Steinhauer, S., Dorenbos, S.N., Sander, N., and Zwiller, V. (2021). Superconducting nanowire single-photon detectors: A perspective on evolution, state-of-the-art, future developments, and applications. *Appl. Phys. Lett.* 118, 190502. <https://doi.org/10.1063/5.0045990>.
  34. Renema, J.J., Gaudio, R., Wang, Q., Zhou, Z., Gaggero, A., Mattioli, F., Leoni, R., Sahin, D., de Dood, M.J.A., Fiore, A., and van Exter, M.P. (2014). Experimental test of theories of the detection mechanism in a nanowire superconducting single photon detector. *Phys. Rev. Lett.* 112, 117604. <https://doi.org/10.1103/PhysRevLett.112.117604>.
  35. Dang, H., Wu, D., Tan, H., Tan, J., Zhai, Y., Wu, S., Ma, D., and Xue, R. (2024). Advances in cryogenic systems for the superconducting nanowire single photon detector and superconducting quantum computer. *IEEE Trans. Appl. Supercond.* 34, 1–4. <https://doi.org/10.1109/TASC.2024.3350594>.
  36. Holzman, I., and Ivry, Y. (2019). Superconducting nanowires for single-photon detection: Progress, challenges, and opportunities. *Adv. Quant. Technol.* 2, 1800058. <https://doi.org/10.1002/quite.201800058>.
  37. Allmaras, J.P. (2020). Modeling and Development of Superconducting Nanowire Single-Photon Detectors. PhD thesis (California Institute of Technology). <https://doi.org/10.7907/wgak-vs11>.
  38. Yang, J., Kerman, A., Dauler, E., Anant, V., Rosfjord, K., and Berggren, K. (2007). Modeling the electrical and thermal response of superconducting nanowire single-photon detectors. *IEEE Trans. Appl. Supercond.* 17, 581–585. <https://doi.org/10.1109/TASC.2007.898660>.
  39. Semenov, A.D., Nebosis, R.S., Gousev, Y.P., Heusinger, M.A., and Renk, K.F. (1995). Analysis of the nonequilibrium photoresponse of superconducting films to pulsed radiation by use of a two-temperature model. *Phys. Rev. B* 52, 581–590. <https://doi.org/10.1103/PhysRevB.52.581>.
  40. Kosterlitz, J., and Thouless, D. (1978). Two-dimensional physics. *Progress Low Temp. Phys.* 7, 371–433. [https://doi.org/10.1016/S0079-6417\(08\)00175-4](https://doi.org/10.1016/S0079-6417(08)00175-4).
  41. Wang, Z., Chaudhary, G., Chen, Q., and Levin, K. (2020). Quantum geometric contributions to the BKT transition: Beyond mean field theory. *Phys. Rev. B* 102, 184504. <https://doi.org/10.1103/PhysRevB.102.184504>.
  42. Kadin, A.M., Epstein, K., and Goldman, A.M. (1983). Renormalization and the Kosterlitz-Thouless transition in a two-dimensional superconductor. *Phys. Rev. B* 27, 6691–6702. <https://doi.org/10.1103/PhysRevB.27.6691>.
  43. Matsuda, Y., Komiyama, S., Onogi, T., Terashima, T., Shimura, K., and Bando, Y. (1993). Thickness dependence of the Kosterlitz-Thouless transition in ultrathin  $\text{YBa}_2\text{Cu}_3\text{O}_{7-x}$  films. *Phys. Rev. B* 48, 498. <https://doi.org/10.1103/PhysRevB.48.10498>.
  44. Bezryadin, A., Lau, C., and Tinkham, M. (2000). Quantum suppression of superconductivity in ultrathin nanowires. *Nature* 404, 971–974. <https://doi.org/10.1038/35010060>.
  45. Jahani, S., Yang, L.-P., Tepole, A.B., Bardin, J.C., Tang, H.X., and Jacob, Z. (2020). Probabilistic vortex crossing criterion for superconducting nanowire single-photon detectors. *J. Appl. Phys.* 127, 143101. <https://doi.org/10.1063/1.5132961>.
  46. Ma, R., Huan, Q., Huang, J., Zhang, X., Xiao, Y., Xu, H., Han, H., Liu, X., Peng, W., Li, H., et al. (2024). Disorder enhanced relative intrinsic detection efficiency in NbTiN superconducting nanowire single photon detectors at high temperature. *Appl. Phys. Lett.* 124, 072601. <https://doi.org/10.1063/5.0190139>.
  47. Jiang, H., Huang, Y., How, H., Zhang, S., Vittoria, C., Widom, A., Christey, D.B., Horowitz, J.S., and Lee, R. (1991). Observation of ultrahigh critical current densities in high- $T_c$  superconducting bridge constrictions. *Phys. Rev. Lett.* 66, 1785–1788. <https://doi.org/10.1103/PhysRevLett.66.1785>.
  48. Pernice, W.H.P., Schuck, C., Minaeva, O., Li, M., Goltzman, G.N., Sergienko, A.V., and Tang, H.X. (2012). High-speed and high-efficiency travelling wave single-photon detectors embedded in nanophotonic circuits. *Nat. Commun.* 3, 1325. <https://doi.org/10.1038/ncomms2307>.
  49. Calandri, N., Zhao, Q.-Y., Zhu, D., Dane, A., and Berggren, K.K. (2016). Superconducting nanowire detector jitter limited by detector geometry. *Appl. Phys. Lett.* 109, 152601. <https://doi.org/10.1063/1.4963158>.
  50. Annunziata, A.J., Quaranta, O., Santavicca, D.F., Casaburi, A., Frunzio, L., Ejrnaes, M., Rooks, M.J., Cristiano, R., Pagano, S., Frydman, A., and Prober, D.E. (2010). Reset dynamics and latching in niobium superconducting nanowire single-photon detectors. *J. Appl. Phys.* 108, 084507. <https://doi.org/10.1063/1.3498809>.
  51. Ejrnaes, M., Casaburi, A., Quaranta, O., Marchetti, S., Gaggero, A., Mattioli, F., Leoni, R., Pagano, S., and Cristiano, R. (2009). Characterization of parallel superconducting nanowire single photon detectors. *Supercond. Sci. Technol.* 22, 055006. <https://doi.org/10.1088/0953-2048/22/5/055006>.
  52. Litombe, N.E., Bollinger, A., Hoffman, J.E., and Božović, I. (2014).  $\text{La}_{2-x}\text{Sr}_x\text{CuO}_4$  superconductor nanowire devices. *Physica C* 506, 169–173. <https://doi.org/10.1016/j.physc.2014.06.010>.
  53. Papari, G., Carillo, F., Stornaiuolo, D., Massarotti, D., Longobardi, L., Beltram, F., and Tafuri, F. (2014). Dynamics of vortex matter in YBCO sub-micron bridges. *Physica C* 506, 188–194. <https://doi.org/10.1016/j.physc.2014.06.017>.
  54. Arpaia, R., Golubev, D., Baghdadi, R., Ciancio, R., Dražić, G., Orgiani, P., Montemurro, D., Bauch, T., and Lombardi, F. (2017). Transport properties of ultrathin  $\text{YBa}_2\text{Cu}_3\text{O}_{7-\delta}$  nanowires: A route to single-photon detection. *Phys. Rev. B* 96, 064525. <https://doi.org/10.1103/PhysRevB.96.064525>.
  55. Arpaia, R., Ejrnaes, M., Parlato, L., Tafuri, F., Cristiano, R., Golubev, D., Sobolewski, R., Bauch, T., Lombardi, F., and Pepe, G.P. (2015). High-temperature superconducting nanowires for photon detection. *Physica C* 509, 16–21. <https://doi.org/10.1016/j.physc.2014.09.017>.
  56. Shibata, H., Takesue, H., Honjo, T., Akazaki, T., and Tokura, Y. (2010). Single-photon detection using magnesium diboride superconducting nanowires. *Appl. Phys. Lett.* 97, 212504. <https://doi.org/10.1063/1.3518723>.

57. Marsili, F., Najafi, F., Dauler, E., Bellei, F., Hu, X., Csete, M., Molnar, R.J., and Berggren, K.K. (2011). Single-photon detectors based on ultranarrow superconducting nanowires. *Nano Lett.* 11, 2048–2053. <https://doi.org/10.1021/nl2005143>.
58. Lyatti, M., Savenko, A., and Poppe, U. (2016). Ultra-thin YBa<sub>2</sub>Cu<sub>3</sub>O<sub>7-x</sub> films with high critical current density. *Supercond. Sci. Technol.* 29, 065017. <https://doi.org/10.1088/0953-2048/29/6/065017>.
59. Chiles, J., Buckley, S.M., Lita, A., Verma, V.B., Allmaras, J., Korzh, B., Shaw, M.D., Shainline, J.M., Mirin, R.P., and Nam, S.W. (2020). Superconducting microwire detectors based on WSi with single-photon sensitivity in the near-infrared. *Appl. Phys. Lett.* 116, 242602. <https://doi.org/10.1063/5.0006221>.
60. Charaev, I., Morimoto, Y., Dane, A., Agarwal, A., Colangelo, M., and Berggren, K.K. (2020). Large-area microwire MoSi single-photon detectors at 1550 nm wavelength. *Appl. Phys. Lett.* 116, 242603. <https://doi.org/10.1063/5.0005439>.
61. Alfieri, A., Anantharaman, S.B., Zhang, H., and Jariwala, D. (2023). Nanomaterials for quantum information science and engineering. *Adv. Mater.* 35, 2109621. <https://doi.org/10.1002/adma.202109621>.
62. Hannachi, E., Almessiere, M.A., Slimani, Y., Alshamrani, R.B., Yasin, G., and Ben Azzouz, F. (2021). Preparation and characterization of high-Tc (YBa<sub>2</sub>Cu<sub>3</sub>O<sub>7-δ</sub>) 1-x/(CNTs) x superconductors with highly boosted superconducting performances. *Ceramics Intern.* 47, 23539–23548. <https://doi.org/10.1016/j.ceramint.2021.05.071>.
63. Chang, J., Gao, J., Esmaili Zadeh, I., Elshaari, A.W., and Zwiller, V. (2023). Nanowire-based integrated photonics for quantum information and quantum sensing. *Nanophotonics* 12, 339–358. <https://doi.org/10.1515/nanoph-2022-0652>.
64. Ejraes, M., Casaburi, A., Quaranta, O., Marchetti, S., Gaggero, A., Mattioli, F., Leoni, R., Pagano, S., and Cristiano, R. (2009). Characterization of parallel superconducting nanowire single photon detectors. *Supercond. Sci. Technol.* 22, 055006. <https://doi.org/10.1088/0953-2048/22/5/055006>.
65. Sriram, M.A., Kumta, P.N., and Ko, E.I. (1995). Interaction of solvent and the nature of adducts on the chemical synthesis of molybdenum nitride powders. *Chem. Mater.* 7, 859–864.
66. Agrafiotis, C.C., Puszynski, J.A., and Hlavacek, V. (1991). Effect of metal particle morphology on the combustion of refractory metals in nitrogen. *J. Am. Ceram. Soc.* 74, 2912–2917. <https://doi.org/10.1111/j.1521-2916.1991.tb06862.x>.
67. Buscaglia, V., Caracciolo, F., Ferretti, M., Minguzzi, M., and Musenich, R. (1998). Effect of pressure on the composition and superconducting Tc value of NbN prepared by combustion synthesis. *J. Alloys Compd.* 266, 201–206. [https://doi.org/10.1016/S0925-8388\(97\)00482-9](https://doi.org/10.1016/S0925-8388(97)00482-9).
68. Kornev, A., Kouminov, P., Matvienko, V., Chulkova, G., Smirnov, K., Voronov, B., Gol'tsman, G.N., Currie, M., Lo, W., Wilsher, K., et al. (2004). Sensitivity and gigahertz counting performance of NbN superconducting single-photon detectors. *Appl. Phys. Lett.* 84, 5338–5340. <https://doi.org/10.1063/1.1764600>.
69. Kerman, A.J., Dauler, E.A., Keicher, W.E., Yang, J.K.W., Berggren, K.K., Gol'tsman, G., and Voronov, B. (2006). Kinetic-inductance-limited reset time of superconducting nanowire photon counters. *Appl. Phys. Lett.* 88, 111116. <https://doi.org/10.1063/1.2183810>.
70. Fabbricatore, P., Fernandes, P., Gualco, G.C., Merlo, F., Musenich, R., and Parodi, R. (1989). Study of niobium nitrides for superconducting rf cavities. *J. Appl. Phys.* 66, 5944–5949. <https://doi.org/10.1063/1.343621>.
71. Kawamura, J., Blundell, R., Tong, C.Y.E., Gol'tsman, G., Gershenson, E., and Voronov, B. (1996). Performance of NbN lattice-cooled hot-electron bolometric mixers. *J. Appl. Phys.* 80, 4232–4234. <https://doi.org/10.1063/1.36330472>.
72. Hajenius, M., Baselmans, J.J.A., Gao, J.R., Klapwijk, T.M., Korte, P.A.J.d., Voronov, B., and Gol'tsman, G. (2004). Low noise NbN superconducting hot electron bolometer mixers at 1.9 and 2.5 THz. *Supercond. Sci. Technol.* 17, S224–S228. <https://doi.org/10.1088/0953-2048/17/5/026>.
73. Rosfjord, K.M., Yang, J.K.W., Dauler, E.A., Kerman, A.J., Anant, V., Voronov, B.M., Gol'tsman, G.N., and Berggren, K.K. (2006). Nanowire single-photon detector with an integrated optical cavity and anti-reflection coating. *Opt Express* 14, 527–534. <https://doi.org/10.1364/OPEX.14.000527>.
74. Stern, J.A., and Farr, W.H. (2007). Fabrication and characterization of superconducting NbN nanowire single photon detectors. *IEEE Trans. Appl. Supercond.* 17, 306–309. <https://doi.org/10.1109/TASC.2007.898060>.
75. Huang, J., Zhang, W., You, L., Zhang, C., Lv, C., Wang, Y., Liu, X., Li, H., and Wang, Z. (2018). High speed superconducting nanowire single-photon detector with nine interleaved nanowires. *Supercond. Sci. Technol.* 31, 074001. <https://doi.org/10.1088/1361-6668/aa1c180>.
76. Kerman, A.J., Yang, J.K.W., Molnar, R.J., Dauler, E.A., and Berggren, K.K. (2009). Electrothermal feedback in superconducting nanowire single-photon detectors. *Phys. Rev. B* 79, 100509. <https://doi.org/10.1103/PhysRevB.79.100509>.
77. Rosenberg, D., Kerman, A.J., Molnar, R.J., and Dauler, E.A. (2013). High-speed and high-efficiency superconducting nanowire single photon detector array. *Opt Express* 21, 1440–1447. <https://doi.org/10.1364/OE.21.001440>.
78. Wu, J.J., You, L.X., Zhang, L., Zhang, W.J., Li, H., Liu, X.Y., Zhou, H., Wang, Z., Xie, X.M., Xu, Y.X., et al. (2016). NbN superconducting nanowire single-photon detector fabricated on MgF<sub>2</sub> substrate. *Supercond. Sci. Technol.* 29, 065011. <https://doi.org/10.1088/0953-2048/29/6/065011>.
79. Miki, S., Yamashita, T., Fujiwara, M., Sasaki, M., and Wang, Z. (2010). Multichannel SNSPD system with high detection efficiency at telecommunication wavelength. *Opt. Lett.* 35, 2133–2135. <https://doi.org/10.1364/OL.35.002133>.
80. Yamashita, T., Miki, S., Terai, H., and Wang, Z. (2013). Low-filling-factor superconducting single photon detector with high system detection efficiency. *Opt Express* 21, 27177–27184. <https://doi.org/10.1364/OE.21.027177>.
81. Wang, Q., Renema, J.J., Engel, A., and de Dood, M. (2017). Design of NbN superconducting nanowire single-photon detectors with enhanced infrared detection efficiency. *Phys. Rev. Appl.* 8, 034004. <https://doi.org/10.1103/PhysRevApplied.8.034004>.
82. Zhang, L., You, L., Yang, X., Wu, J., Lv, C., Guo, Q., Zhang, W., Li, H., Peng, W., Wang, Z., and Xie, X. (2018). Hotspot relaxation time of NbN superconducting nanowire single-photon detectors on various substrates. *Sci. Rep.* 8, 1486. <https://doi.org/10.1038/s41598-018-20035-7>.
83. Verevkina, A., Pearlman, A., Slysz, W., Zhang, J., Currie, M., Kornev, A., Chulkova, G., Okunev, O., Kouminov, P., Smirnov, K., et al. (2004). Ultrafast superconducting single-photon detectors for near-infrared-wavelength quantum communications. *J. Mod. Opt.* 51, 1447–1458. <https://doi.org/10.1080/09500340408235284>.
84. Hadfield, R.H., Habif, J.L., Schlafer, J., Schwall, R.E., and Nam, S.W. (2006). Quantum key distribution at 1550 nm with twin superconducting single-photon detectors. *Appl. Phys. Lett.* 89, 241129. <https://doi.org/10.1063/1.2405870>.
85. Tanaka, A., Fujiwara, M., Nam, S.W., Nambu, Y., Takahashi, S., Maeda, W., Yoshino, K.i., Miki, S., Baek, B., Wang, Z., et al. (2008). Ultra fast quantum key distribution over a 97 km installed telecom fiber with wavelength division multiplexing clock synchronization. *Opt Express* 16, 11354–11360. <https://doi.org/10.1364/OE.16.011354>.
86. Hayashi, M. (2007). Upper bounds of eavesdropper's performances in finite-length code with the decoy method. *Phys. Rev. A* 76, 012329. <https://doi.org/10.1103/PhysRevA.76.012329>.
87. Hayashi, M. (2007). General theory for decoy-state quantum key distribution with an arbitrary number of intensities. *New J. Phys.* 9, 284. <https://doi.org/10.1088/1367-2630/9/8/284>.
88. Honjo, T., Nam, S.W., Takesue, H., Zhang, Q., Kamada, H., Nishida, Y., Tadanaga, O., Asobe, M., Baek, B., Hadfield, R., et al. (2008). Long-distance entanglement-based quantum key distribution over optical fiber. *Opt Express* 16, 19118–19126. <https://doi.org/10.1364/OE.16.019118>.
89. Stucki, D., Walenta, N., Vannel, F., Thew, R.T., Gisin, N., Zbinden, H., Gray, S., Towery, C.R., and Ten, S. (2009). High rate, long-distance quantum key distribution over 250 km of ultra low loss fibres. *New J. Phys.* 11, 075003. <https://doi.org/10.1088/1367-2630/11/7/075003>.
90. Cheng, R., Wang, S., and Tang, H.X. (2019). Superconducting nanowire single-photon detectors fabricated from atomic-layer-deposited NbN. *Appl. Phys. Lett.* 115, 241101. <https://doi.org/10.1063/1.5131664>.
91. Knehr, E., Kuzmin, A., Vodolazov, D.Y., Ziegler, M., Doerner, S., Ilin, K., Siegel, M., Stolz, R., and Schmidt, H. (2019). Nanowire single-photon detectors made of atomic layer-deposited niobium nitride. *Supercond. Sci. Technol.* 32, 125007. <https://doi.org/10.1088/1361-6668/ab48d7>.
92. Miki, S., Fujiwara, M., Sasaki, M., Baek, B., Miller, A.J., Hadfield, R.H., Nam, S.W., and Wang, Z. (2008). Large sensitive-area NbN nanowire superconducting single-photon detectors fabricated on single-crystal MgO substrates. *Appl. Phys. Lett.* 92, 061116. <https://doi.org/10.1063/1.2870099>.

93. Dane, A.E., McCaughan, A.N., Zhu, D., Zhao, Q., Kim, C.S., Calandri, N., Agarwal, A., Bellei, F., and Berggren, K.K. (2017). Bias sputtered NbN and superconducting nanowire devices. *Appl. Phys. Lett.* 111, 122601. <https://doi.org/10.1063/1.4990066>.
94. Delacour, C., Claudon, J., Poizat, J.P., Pannetier, B., Bouchiat, V., Espiau de Lamaestre, R., Villegier, J.C., Tarkhov, M., Korneev, A., Voronov, B., and Gol'tsman, G. (2007). Superconducting single photon detectors made by local oxidation with an atomic force microscope. *Appl. Phys. Lett.* 90, 191116. <https://doi.org/10.1063/1.2738195>.
95. Yang, M., Liu, L.H., Ning, L.H., Jin, Y.R., Deng, H., Li, J., Li, Y., and Zheng, D.N. (2016). Fabrication of superconducting NbN meander nanowires by nano-imprint lithography. *Chin. Phys. B* 25, 017401. <https://doi.org/10.1088/1674-1056/25/1/017401>.
96. Minaev, N.V., Tarkhov, M.A., Dudova, D.S., Timashev, P.S., Chichkov, B.N., and Bagratashvili, V.N. (2018). Fabrication of superconducting nanowire single-photon detectors by nonlinear femtosecond optical lithography. *Laser Phys. Lett.* 15, 026002. <https://doi.org/10.1088/1612-202X/aa8bd1>.
97. Korneeva, Y.P., Vodolazov, D.Y., Semenov, A.V., Florya, I.N., Simonov, N., Baeva, E., Korneev, A.A., Goltsman, G.N., and Klapwijk, T.M. (2018). Optical single-photon detection in micrometer-scale NbN bridges. *Phys. Rev. Appl.* 9, 064037. <https://doi.org/10.1103/PhysRevApplied.9.064037>.
98. Jia, T., Kang, L., Zhang, L., Zhao, Q., Gu, M., Qiu, J., Chen, J., and Jin, B. (2014). Doped niobium superconducting nanowire single-photon detectors. *Appl. Phys. B* 116, 991–995. <https://doi.org/10.1007/s00340-014-5787-0>.
99. Jia, X.Q., Kang, L., Gu, M., Yang, X.Z., Chen, C., Tu, X.C., Jin, B.B., Xu, W.W., Chen, J., and Wu, P.H. (2014). Fabrication of a strain-induced high performance NbN ultrathin film by a Nb5N6 buffer layer on Si substrate. *Supercond. Sci. Technol.* 27, 035010. <https://doi.org/10.1088/0953-2048/27/3/035010>.
100. Xu, T., Chen, S., Shi, H.K., Jia, X.Q., Zhang, L.B., Zhao, Q.Y., Tu, X.C., Kang, L., Chen, J., and Wu, P.H. (2021). Effect of buffer layer on thermal recovery of superconducting nanowire single-photon detector. *Supercond. Sci. Technol.* 34, 074002. <https://doi.org/10.1088/1361-6668/ac0015>.
101. Dorenbos, S.N., Reiger, E.M., Perinetti, U., Zwiller, V., Zijlstra, T., and Klapwijk, T.M. (2008). Low noise superconducting single photon detectors on silicon. *Appl. Phys. Lett.* 93, 131101. <https://doi.org/10.1063/1.2990646>.
102. Miki, S., Takeda, M., Fujiwara, M., Sasaki, M., Otomo, A., and Wang, Z. (2009). Superconducting NbTiN nanowire single photon detectors with low kinetic inductance. *Appl. Phys. Express* 2, 075002. <https://doi.org/10.1143/APEX.2.075002>.
103. Tanner, M.G., Natarajan, C.M., Pottapenjara, V.K., O'Connor, J.A., Warburton, R.J., Hadfield, R.H., Baek, B., Nam, S., Dorenbos, S.N., Ureña, E.B., et al. (2010). Enhanced telecom wavelength single-photon detection with NbTiN superconducting nanowires on oxidized silicon. *Appl. Phys. Lett.* 96, 221109. <https://doi.org/10.1063/1.3428960>.
104. Zichi, J., Chang, J., Steinhauer, S., Von Fieandt, K., Los, J.W.N., Visser, G., Kalhor, N., Lettner, T., Elshaari, A.W., Zadeh, I.E., and Zwiller, V. (2019). Optimizing the stoichiometry of ultrathin NbTiN films for high-performance superconducting nanowire single-photon detectors. *Opt. Express* 27, 26579–26587. <https://doi.org/10.1364/OE.27.026579>.
105. Eraerts, P., Legré, M., Zhang, J., Zbinden, H., and Gisin, N. (2010). Photon counting OTDR: advantages and limitations. *J. Lightwave Technol.* 28, 952–964. <https://doi.org/10.1109/JLT.2009.2039635>.
106. Takesue, H., Nam, S.W., Zhang, Q., Hadfield, R.H., Honjo, T., Tamaki, K., and Yamamoto, Y. (2007). Quantum key distribution over a 40-dB channel loss using superconducting single-photon detectors. *Nat. Photonics* 1, 343–348. <https://doi.org/10.1038/nphoton.2007.75>.
107. Gisin, N., Ribordy, G., Tittel, W., and Zbinden, H. (2002). Quantum cryptography. *Rev. Mod. Phys.* 74, 145–195. <https://doi.org/10.1103/RevModPhys.74.145>.
108. Schuck, C., Pernice, W.H.P., and Tang, H.X. (2013). Waveguide integrated low noise NbTiN nanowire single-photon detectors with milli-Hz dark count rate. *Sci. Rep.* 3, 1893. <https://doi.org/10.1038/srep01893>.
109. Jia, X., Kang, L., Yang, X., Wang, Z., Ren, T., Jin, B.B., Xu, W., Chen, J., and Wu, P. (2014). Ultrathin NbTiN films with high Ti composition for superconducting nanowire single photon detectors. *IEEE Trans. Appl. Supercond.* 25, 1–4. <https://doi.org/10.1109/TASC.2014.2373818>.
110. Gourgues, R., Los, J.W.N., Zichi, J., Chang, J., Kalhor, N., Bulgarini, G., Dorenbos, S.N., Zwiller, V., and Zadeh, I.E. (2019). Superconducting nanowire single photon detectors operating at temperature from 4 to 7 K. *Opt Express* 27, 24601–24609. <https://doi.org/10.1364/OE.27.024601>.
111. Zadeh, I.E., Los, J.W., Gourgues, R., Steinmetz, V., Bulgarini, G., Dobrovolskiy, S.M., Zwiller, V., and Dorenbos, S.N. (2017). Single-photon detectors combining high efficiency, high detection rates, and ultra-high timing resolution. *APL Photonics* 2, 11. <https://doi.org/10.1063/1.5000001>.
112. Esmaili Zadeh, I., Los, J.W.N., Gourgues, R.B.M., Chang, J., Elshaari, A.W., Zichi, J.R., Van Staaden, Y.J., Swens, J.P.E., Kalhor, N., Guardiani, A., et al. (2020). Efficient single-photon detection with 7.7 ps time resolution for photon-correlation measurements. *ACS Photonics* 7, 1780–1787. <https://doi.org/10.1021/acspophotonics.0c00433>.
113. Chang, J., Los, J.W.N., Tenorio-Pearl, J.O., Noordzij, N., Gourgues, R., Guardiani, A., Zichi, J.R., Pereira, S.F., Urbach, H.P., Zwiller, V., et al. (2021). Detecting telecom single photons with 99.5–2.07+0.5% system detection efficiency and high time resolution. *APL Photonics* 6, 036114. <https://doi.org/10.1063/5.0039772>.
114. Chang, J., Los, J.W.N., Gourgues, R., Steinhauer, S., Dorenbos, S.N., Pereira, S.F., Urbach, H.P., Zwiller, V., and Esmaili Zadeh, I. (2022). Efficient mid-infrared single-photon detection using superconducting NbTiN nanowires with high time resolution in a Gifford-McMahon cryocooler. *Photon. Res.* 10, 1063–1070. <https://doi.org/10.1364/PRJ.437834>.
115. Chang, J., Zadeh, I.E., Los, J.W.N., Zichi, J., Fognini, A., Gevers, M., Dorenbos, S., Pereira, S.F., Urbach, P., and Zwiller, V. (2019). Multimode-fiber-coupled superconducting nanowire single-photon detectors with high detection efficiency and time resolution. *Appl. Opt.* 58, 9803–9807. <https://doi.org/10.1364/AO.58.009803>.
116. Cirillo, C., Chang, J., Caputo, M., Los, J.W.N., Dorenbos, S., Esmaili Zadeh, I., and Attanasio, C. (2020). Superconducting nanowire single photon detectors based on disordered NbRe films. *Appl. Phys. Lett.* 117, 172602. <https://doi.org/10.1063/5.0021487>.
117. Rossnagel, S.M. (2002). Characteristics of ultrathin Ta and TaN films. *J. Vac. Sci. Technol. B Microelectron. Nanometer Struct. Process. Meas. Phenom.* 20, 2328–2336. <https://doi.org/10.1116/1.1520556>.
118. Setzu, R., Baggetta, E., and Villegier, J.C. (2008). Study of NbN Josephson junctions with a tantalum nitride barrier tuned to the metal-insulator transition. *J. Phys.: Conf. Ser.* 97, 012077. <https://doi.org/10.1088/1742-6596/97/1/012077>.
119. Il'in, K., Hofherr, M., Rall, D., Siegel, M., Semenov, A., Engel, A., Inderbitzin, K., Aeschbacher, A., and Schilling, A. (2012). Ultra-thin TaN films for superconducting nanowire single-photon detectors. *J. Low Temp. Phys.* 167, 809–814. <https://doi.org/10.1007/s10909-011-0424-3>.
120. Engel, A., Aeschbacher, A., Inderbitzin, K., Schilling, A., Il'in, K., Hofherr, M., Siegel, M., Semenov, A., and Hübers, H.W. (2012). Tantalum nitride superconducting single-photon detectors with low cut-off energy. *Appl. Phys. Lett.* 100, 062601. <https://doi.org/10.1063/1.3684243>.
121. Engel, A., Inderbitzin, K., Schilling, A., Lusche, R., Semenov, A., Hübers, H.W., Henrich, D., Hofherr, M., Il'in, K., and Siegel, M. (2013). Temperature-dependence of detection efficiency in NbN and TaN SNSPD. *IEEE Trans. Appl. Supercond.* 23, 2300505. <https://doi.org/10.1109/TASC.2013.2239345>.
122. Korneeva, Y., Florya, I., Vdovichev, S., Moshkova, M., Simonov, N., Kaurova, N., Korneev, A., and Goltsman, G. (2017). Comparison of hot spot formation in NbN and MoN thin superconducting films after photon absorption. *IEEE Trans. Appl. Supercond.* 27, 1–4. <https://doi.org/10.1109/TASC.2017.2659661>.
123. Evtikhiev, N.N., Kurbatova, E.A., and Cherenkhin, P.A. (2018). Coefficients quantization at off-axis digital hologram wavelet compression. *KEN Energy* 3, 523–534. <https://doi.org/10.18502/ken.v3i3.2066>.
124. Chen, J., Altepeter, J.B., Medic, M., Lee, K.F., Gokden, B., Hadfield, R.H., Nam, S.W., and Kumar, P. (2008). Demonstration of a quantum controlled-NOT gate in the telecommunications band. *Phys. Rev. Lett.* 100, 133603. <https://doi.org/10.1103/PhysRevLett.100.133603>.
125. Clausen, C., Usmani, I., Bussières, F., Sangouard, N., Afzelius, M., De Riedmatten, H., and Gisin, N. (2011). Quantum storage of photonic entanglement in a crystal. *Nature* 469, 508–511. <https://doi.org/10.1038/nature09662>.
126. Correa, R.E., Dauler, E.A., Nair, G., Pan, S.H., Rosenberg, D., Kerman, A.J., Molnar, R.J., Hu, X., Marsili, F., Anant, V., et al. (2012). Single photon counting from individual nanocrystals in the infrared. *Nano Lett.* 12, 2953–2958. <https://doi.org/10.1021/nl300642k>.

127. Toth, L. (2014). *Transition Metal Carbides and Nitrides* (Elsevier).
128. Kerman, A.J., Dauler, E.A., Yang, J.K.W., Rosfjord, K.M., Anant, V., Berggren, K.K., Gol'tsman, G.N., and Voronov, B.M. (2007). Constriction-limited detection efficiency of superconducting nanowire single-photon detectors. *Appl. Phys. Lett.* 90, 101110. <https://doi.org/10.1063/1.2696926>.
129. Baek, B., Lita, A.E., Verma, V., and Nam, S.W. (2011). Superconducting a  $W_xSi_{1-x}$  nanowire single-photon detector with saturated internal quantum efficiency from visible to 1850 nm. *Appl. Phys. Lett.* 98, 251105. <https://doi.org/10.1063/1.3600793>.
130. Marsili, F., Verma, V.B., Stern, J.A., Harrington, S., Lita, A.E., Gerrits, T., Vayshenker, I., Baek, B., Shaw, M.D., Mirin, R.P., and Nam, S.W. (2013). Detecting single infrared photons with 93% system efficiency. *Nat. Photonics* 7, 210–214. <https://doi.org/10.1038/nphoton.2013.13>.
131. Verma, V.B., Lita, A.E., Vissers, M.R., Marsili, F., Pappas, D.P., Mirin, R.P., and Nam, S.W. (2014). Superconducting nanowire single photon detectors fabricated from an amorphous  $Mo_{0.75}Ge_{0.25}$  thin film. *Appl. Phys. Lett.* 105, 022602. <https://doi.org/10.1063/1.4890277>.
132. Verma, V.B., Korzh, B., Bussières, F., Horansky, R.D., Lita, A.E., Marsili, F., Shaw, M.D., Zbinden, H., Mirin, R.P., and Nam, S.W. (2014). High-efficiency WSi superconducting nanowire single-photon detectors operating at 2.5 K. *Appl. Phys. Lett.* 105, 122601. <https://doi.org/10.1063/1.4890405>.
133. Allmaras, J.P., Kozorezov, A.G., Beyer, A.D., Marsili, F., Briggs, R.M., and Shaw, M.D. (2018). Thin-Film Thermal Conductivity Measurements Using Superconducting Nanowires. *J. Low Temp. Phys.* 193, 380–386. <https://doi.org/10.1007/s10909-018-2022-0>.
134. Dorenbos, S.N., Forn-Díaz, P., Fuse, T., Verbruggen, A.H., Zijlstra, T., Klapwijk, T.M., and Zwiller, V. (2011). Low gap superconducting single photon detectors for infrared sensitivity. *Appl. Phys. Lett.* 98, 251102. <https://doi.org/10.1063/1.3599712>.
135. Korneeva, Y.P., Mikhailov, M.Y., Pershin, Y.P., Manova, N.N., Divochiy, A.V., Vakhtomin, Y.B., Korneev, A.A., Smirnov, K.V., Sivakov, A.G., Devizenko, A.Y., and Goltsman, G.N. (2014). Superconducting single-photon detector made of MoSi film. *Supercond. Sci. Technol.* 27, 095012. <https://doi.org/10.1088/0953-2048/27/9/095012>.
136. Smith, A.W., Clinton, T.W., Tsuei, C.C., and Lobb, C.J. (1994). Sign reversal of the Hall resistivity in amorphous Mo 3 Si. *Phys. Rev. B* 49, 12927–12930. <https://doi.org/10.1103/PhysRevB.49.12927>.
137. Kubo, S. (1988). Superconducting properties of amorphous MoX (X= Si, Ge) alloy films for Abrikosov vortex memory. *J. Appl. Phys.* 53, 2033–2045. <https://doi.org/10.1063/1.341105>.
138. Lita, A.E., Verma, V.B., Horansky, R.D., Shainline, J.M., Mirin, R.P., and Nam, S. (2015). Materials development for high efficiency superconducting nanowire single-photon detectors. *MRS Proc.* 1807, 1–6. <https://doi.org/10.1557/opl.2015.544>.
139. Verma, V.B., Korzh, B., Bussières, F., Horansky, R.D., Dyer, S.D., Lita, A.E., Vayshenker, I., Marsili, F., Shaw, M.D., Zbinden, H., et al. (2015). High-efficiency superconducting nanowire single-photon detectors fabricated from MoSi thin-films. *Opt Express* 23, 33792–33801. <https://doi.org/10.1364/OE.23.033792>.
140. Li, J., Kirkwood, R.A., Baker, L.J., Bosworth, D., Erotokritou, K., Banerjee, A., Heath, R.M., Natarajan, C.M., Barber, Z.H., Sorel, M., and Hadfield, R.H. (2016). Nano-optical single-photon response mapping of waveguide integrated molybdenum silicide (MoSi) superconducting nanowires. *Opt Express* 24, 13931–13938. <https://doi.org/10.1364/OE.24.013931>.
141. Banerjee, A., Baker, L.J., Doye, A., Nord, M., Heath, R.M., Erotokritou, K., Bosworth, D., Barber, Z.H., MacLaren, I., and Hadfield, R.H. (2017). Characterisation of amorphous molybdenum silicide (MoSi) superconducting thin films and nanowires. *Supercond. Sci. Technol.* 30, 084010. <https://doi.org/10.1088/1361-6668/aa76d8>.
142. Wollman, E.E., Verma, V.B., Beyer, A.D., Briggs, R.M., Korzh, B., Allmaras, J.P., Marsili, F., Lita, A.E., Mirin, R.P., Nam, S.W., and Shaw, M.D. (2017). UV superconducting nanowire single-photon detectors with high efficiency, low noise, and 4 K operating temperature. *Opt Express* 25, 26792–26801. <https://doi.org/10.1364/OE.25.026792>.
143. Miki, S., Yamashita, T., Terai, H., and Wang, Z. (2013). High performance fiber-coupled NbTiN superconducting nanowire single photon detectors with Gifford-McMahon cryocooler. *Opt Express* 21, 10208–10214. <https://doi.org/10.1364/OE.21.010208>.
144. Verma, V.B., Marsili, F., Harrington, S., Lita, A.E., Mirin, R.P., and Nam, S.W. (2012). A three-dimensional, polarization-insensitive superconducting nanowire avalanche photodetector. *Appl. Phys. Lett.* 101, 251114. <https://doi.org/10.1063/1.4768788>.
145. Day, C. (2001). New Conventional Superconductor Found with a Surprisingly High T<sub>c</sub>. *Phys. Today* 54, 17–18. <https://doi.org/10.1063/1.1372100>.
146. Nagamatsu, J., Nakagawa, N., Muranaka, T., Zenitani, Y., and Akimitsu, J. (2001). Superconductivity at 39 K in magnesium diboride. *Nature* 410, 63–64. <https://doi.org/10.1038/35065039>.
147. Eom, C.B., Lee, M.K., Choi, J.H., Belenky, L.J., Song, X., Cooley, L.D., Naus, M.T., Patnaik, S., Jiang, J., Rikel, M., and Polyaniskii, A. (2001). Thin film magnesium diboride superconductor with very high critical current density and enhanced irreversibility field. *Nature* 411, 558–560. <https://doi.org/10.1038/35079018>.
148. Kang, W.N., Kim, H.-J., Choi, E.-M., Jung, C.U., and Lee, S.-I. (2001). MgB<sub>2</sub> superconducting thin films with a transition temperature of 39 Kelvin. *Science* 292, 1521–1523. <https://doi.org/10.1126/science.1060822>.
149. Brinkman, A., Mijatovic, D., Rijnders, G., Leca, V., Smilde, H.J.H., Oomen, I., Golubov, A.A., Roesthuis, F., Harkema, S., Hilgenkamp, H., et al. (2001). Superconducting thin films of MgB<sub>2</sub> on Si by pulsed laser deposition. *Phys. C Supercond.* 353, 1–4. [https://doi.org/10.1016/S0921-4534\(01\)00396-3](https://doi.org/10.1016/S0921-4534(01)00396-3).
150. Monticone, E., Portesi, C., Borini, S., Taralli, E., and Rajteri, M. (2007). Superconducting MgB<sub>2</sub> Nanostructures Fabricated by Electron Beam Lithography. *IEEE Trans. Appl. Supercond.* 17, 222–224. <https://doi.org/10.1109/TASC.2007.898183>.
151. Cherednichenko, S., Acharya, N., Novoselov, E., and Drakinskiy, V. (2021). Low kinetic inductance superconducting MgB<sub>2</sub> nanowires with a 130 ps relaxation time for single-photon detection applications. *Supercond. Sci. Technol.* 34, 044001. <https://doi.org/10.1088/1361-6668/abdeda>.
152. Khafizov, M., Li, X., Cui, Y., Xi, X., and Sobolewski, R. (2007). Mechanism of Light Detection in Current-Biased Superconducting MgB<sub>2</sub> Microbridges. *IEEE Trans. Appl. Supercond.* 17, 2867–2870. <https://doi.org/10.1109/TASC.2007.898372>.
153. Shibata, H., Maruyama, T., Akazaki, T., Takesue, H., Honjo, T., and Tokura, Y. (2008). Photon detection and fabrication of MgB<sub>2</sub> nanowire. *Phys. C Supercond.* 468, 1992–1994. <https://doi.org/10.1016/j.physc.2008.05.248>.
154. Shishido, H., Yoshida, T., and Ishida, T. (2015). Ambient temperature epitaxial growth of MgB<sub>2</sub> thin films with a Mg buffer layer. *Appl. Phys. Express* 8, 113101. <https://doi.org/10.7567/APEX.8.113101>.
155. Shibata, H. (2021). Review of superconducting nanostrip photon detectors using various superconductors. *IEICE Trans. Electron.* E104.C, 429–434. <https://doi.org/10.1587/transele.2020SU0001>.
156. Wang, D., Zhang, C., Zhang, J., Zhang, Y., Feng, Q.R., Wang, Y., and Gan, Z.Z. (2015). Degradation of MgB<sub>2</sub> Ultrathin Films Under Different Environmental Conditions. *IEEE Trans. Appl. Supercond.* 25, 1–9. <https://doi.org/10.1109/TASC.2014.2379722>.
157. Acharya, N., Wolak, M.A., Melbourne, T., Cunnane, D., Karasik, B.S., and Xi, X. (2017). As-grown versus ion-milled MgB<sub>2</sub> ultrathin films for THz sensor applications. *IEEE Trans. Appl. Supercond.* 27, 1–4. <https://doi.org/10.1109/TASC.2016.2645126>.
158. Charaev, I., Batson, E.K., Cherednichenko, S., Reidy, K., Drakinskiy, V., Yu, Y., Lara-Avila, S., Thomsen, J.D., Colangelo, M., Incalza, F., et al. (2024). Single-photon detection using large-scale high-temperature MgB<sub>2</sub> sensors at 20 K. *Nat. Commun.* 15, 3973. <https://doi.org/10.1038/s41467-024-47353-x>.
159. Enomoto, Y., and Murakami, T. (1986). Optical detector using superconducting BaP<sub>0.7</sub>Bi<sub>0.3</sub>O<sub>3</sub> thin films. *J. Appl. Phys.* 59, 3807–3814. <https://doi.org/10.1063/1.336720>.
160. Yoshisato, Y., Takeoka, A., Ikemachi, T., Niki, K., Yokoo, T., Nakano, S., and Kuwano, Y. (1990). Microwave detector using granular-type YBCO superconductors. *Jpn. J. Appl. Phys.* 29, 1080. <https://doi.org/10.1143/JJAP.29.1080>.
161. Leung, M., Broussard, P.R., Claassen, J.H., Osofsky, M., Wolf, S.A., and Strom, U. (1987). Optical detection in thin granular films of Y-Ba-Cu-O at temperatures between 4.2 and 100 K. *Appl. Phys. Lett.* 51, 2046–2047. <https://doi.org/10.1063/1.98287>.
162. Frenkel, A., Saifi, M.A., Venkatesan, T., England, P., Wu, X.D., and Inam, A. (1990). Optical response of nongranular high-T<sub>c</sub>  $Y_1Ba_2Cu_3O_{7-\delta}$  superconducting thin films. *J. Appl. Phys.* 67, 3054–3068. <https://doi.org/10.1063/1.345435>.
163. Carr, G.L., Quijada, M., Tanner, D.B., Hirschmugl, C.J., Williams, G.P., Etemad, S., Dutta, B., DeRosa, F., Inam, A., Venkatesan, T., and Xi, X. (1990). Fast bolometric response by high T<sub>c</sub> detectors measured with subnanosecond synchrotron radiation.

- Appl. Phys. Lett. 57, 2725–2727. <https://doi.org/10.1063/1.103772>.
164. Zheng, J.P., Ying, Q.Y., and Kwok, H.S. (1990). Y-Ba-Cu-O thin film infrared detectors. Phys. C Supercond. 168, 322–326. [https://doi.org/10.1016/0921-4534\(90\)90525-J](https://doi.org/10.1016/0921-4534(90)90525-J).
165. Eidelloth, W. (1991). Optical response of highly oriented YBCO thin films. IEEE Trans. Magn. 27, 2828–2831. <https://doi.org/10.1109/20.133798>.
166. Eidelloth, W., and Barnes, F.S. (1989). Optical response of bulk Bi-Sr-Ca-Cu-O. IEEE J. Quant. Electron. 25, 2405–2409. <https://doi.org/10.1109/3.42073>.
167. Schneider, G., Lengfellner, H., Betz, J., Renk, K.F., and Prettl, W. (1991). Infrared detection by Tl–Ba–Ca–Cu–O superconducting films. Int. J. Infrared. Milli. Waves 12, 1–7. <https://doi.org/10.1007/BF01041878>.
168. Lau, J.A., Verma, V.B., Schwarzer, D., and Wodtke, A.M. (2023). Superconducting single-photon detectors in the mid-infrared for physical chemistry and spectroscopy. Chem. Soc. Rev. 52, 921–941. <https://doi.org/10.1039/D1CS00434D>.
169. Vollman, E.E., Verma, V.B., Walter, A.B., Chiles, J., Korzh, B., Allmaras, J.P., Zhai, Y., Lita, A.E., McCaughan, A.N., Schmidt, E., et al. (2021). Recent advances in superconducting nanowire single-photon detector technology for exoplanet transit spectroscopy in the mid-infrared. J. Astron. Telesc. Instrum. Syst. 7, 11004. <https://doi.org/10.1111/1.JATIS.7.1.011004>.
170. Shibata, H., Kirigane, N., Fukao, K., Sakai, D., Karimoto, S., and Yamamoto, H. (2017). Photoresponse of a La<sub>1.85</sub>Sr<sub>0.15</sub>CuO<sub>4</sub> nanostrip. Supercond. Sci. Technol. 30, 074001. <https://doi.org/10.1088/1361-6668/aa6c3e>.
171. Merino, R.L., Seifert, P., Retamal, J.D., Mech, R.K., Taniguchi, T., Watanabe, K., Kadouki, K., Hadfield, R.H., and Efetov, D.K. (2023). Two-dimensional cuprate nanodetector with single telecom photon sensitivity at T= 20 K. 2D Mater. 10, 021001. <https://doi.org/10.1088/2053-1583/acb4a8>.
172. Charaev, I., Bandurin, D.A., Bollinger, A.T., Phinney, I.Y., Drozdov, I., Colangelo, M., Butters, B.A., Taniguchi, T., Watanabe, K., He, X., et al. (2023). Single-photon detection using high-temperature superconductors. Nat. Nanotechnol. 18, 343–349. <https://doi.org/10.1038/s41565-023-01325-2>.
173. Seifert, P., Retamal, J.R.D., Merino, R.L., Sheinfux, H.H., Moore, J.N., Aamir, M.A., Taniguchi, T., Watanabe, K., Kadouki, K., Artiglia, M., et al. (2021). A high-T<sub>C</sub> van der Waals superconductor based photodetector with ultra-high responsivity and nanosecond relaxation time. 2D Mater. 8, 035053. <https://doi.org/10.1088/2053-1583/ac072f>.
174. Maple, M., de Andrade, M.C., Herrmann, J., Dickey, R.P., Dilley, N.R., and Han, S. (1997). Superconductivity in rare earth and actinide compounds. J. Alloys Compd. 250, 585–595. [https://doi.org/10.1016/S0925-3888\(96\)02832-0](https://doi.org/10.1016/S0925-3888(96)02832-0).
175. Korina, E., Karaberova, A., Bol'shakov, O., Bulatova, E., Golovin, M., Abramyan, A., and Stanković, D.M. (2024). Enhancing Adrenaline Sensing with Lanthanum Cuprate: A Promising Approach for a Novel Sensor. J. Electrochem. Soc. 171, 017513. <https://doi.org/10.1149/1945-7111/ad1ecb>.
176. Johrendt, D. (2020). Rare earth based superconducting materials. Rare Earth Chem. 1, 557. DeGruyter. <https://doi.org/10.1515/9783110654929>.
177. Marzougui, B., Marzouki, A., Smida, Y.B., and Marzouki, R. (2023). The Cuprate Ln<sub>2</sub>CuO<sub>4</sub> (Ln: Rare Earth): Synthesis, Crystallography, and Applications. <https://doi.org/10.5772/intechopen.109193>.
178. Capponi, J.J., Chaillout, C.W., Lejay, P., Ngugen, B., Raveau, J.L., Soubeyroux, J.L., and Tournier, R. (1987). Symmetry classification of states in high temperature superconductors. Europhys. Lett. 3, 13019.
179. Cava, R.J., Batlogg, B., Chen, C.H., Rietman, E.A., Zahurak, S.M., and Werder, D. (1987). Single-phase 60-K bulk superconductor in annealed Ba 2 Y Cu 3 O 7 – δ (0.3 < δ < 0.4) with correlated oxygen vacancies in the Cu-O chains. Phys. Rev. B 36, 5719–5722. <https://doi.org/10.1103/PhysRevB.36.5719>.
180. Jorgensen, J., Veal, B.W., Kwo, W.K., Crabtree, G.W., Umezawa, A., Nowicki, L.J., and Paulikas, A.P. (1987). Structural and superconducting properties of orthorhombic and tetragonal Y Ba 2 Cu 3 O 7 – x: The effect of oxygen stoichiometry and ordering on superconductivity. Phys. Rev. B 36, 5731–5734. <https://doi.org/10.1103/PhysRevB.36.5731>.
181. Thoma, P. (2014). Ultra-fast YBa<sub>2</sub>Cu<sub>3</sub>O<sub>7</sub>-X Direct Detectors for the THz Frequency Range. Vol. 9 (KIT Scientific Publishing).
182. Fournier, P. (2015). T' and infinite-layer electron-doped cuprates. Physica C 514, 314–338. <https://doi.org/10.1016/j.physc.2015.02.036>.
183. Curtz, N., Koller, E., Zbinden, H., Decroux, M., Antognazzi, L., Fischer, Ø., and Gisin, N. (2010). Patterning of ultrathin YBCO nanowires using a new focused-ion-beam process. Supercond. Sci. Technol. 23, 045015. <https://doi.org/10.1088/0953-2048/23/4/045015>.
184. Probst, P., Semenov, A., Ries, M., Hoehl, A., Rieger, P., Scheuring, A., Judin, V., Wünsch, S., Il'in, K., Smale, N., et al. (2012). Nonthermal response of YBa 2 Cu 3 O 7 – δ thin films to picosecond THz pulses. Phys. Rev. B 85, 174511. <https://doi.org/10.1103/PhysRevB.85.174511>.
185. Nawaz, S., Arpaia, R., Lombardi, F., and Bauch, T. (2013). Microwave response of superconducting YBa<sub>2</sub>Cu<sub>3</sub>O<sub>7</sub>-δ nanowire bridges sustaining the critical depairing current: Evidence of Josephson-like behavior. Phys. Rev. Lett. 110, 167004. <https://doi.org/10.1103/PhysRevLett.110.167004>.
186. Amari, P., Feuillet-Palma, C., Jouan, A., Couedo, F., Boulet, N., Géron, E., Malhou, M., Méchin, L., Sharafiev, A., Lesueur, J., and Bergal, N. (2016). Ion Irradiated YBa<sub>2</sub>Cu<sub>3</sub>O<sub>7</sub> Nano-Meanders for Superconducting Single Photon Detectors. <https://doi.org/10.48550/arXiv.1612.07730>.
187. Arpaia, R., Andersson, E., Trabaldo, E., Bauch, T., and Lombardi, F. (2018). Probing the phase diagram of cuprates with YBa 2 Cu 3 O 7 – δ thin films and nanowires. Phys. Rev. Mater. 2, 024804. <https://doi.org/10.1103/PhysRevMaterials.2.024804>.
188. Ejnæs, M., Parlato, L., Arpaia, R., Bauch, T., Lombardi, F., Cristiano, R., Tafuri, F., and Pepe, G.P. (2017). Observation of dark pulses in 10 nm thick YBCO nanostrips presenting hysteretic current voltage characteristics. Supercond. Sci. Technol. 30, 12LT02. <https://doi.org/10.1088/1361-6668/aa94b9>.
189. Lyatti, M., Wolff, M.A., Gundareva, I., Kruth, M., Ferrari, S., Dunin-Borkowski, R.E., and Schuck, C. (2020). Energy-level quantization and single-photon control of phase slips in YBa<sub>2</sub>Cu<sub>3</sub>O<sub>7-x</sub> nanowires. Nature 11, 763. <https://doi.org/10.1038/s41467-020-14548-x>.
190. Kumar, A., Panna, D., Bouscher, S., Koriat, A., Nitav, Y., Jacobi, R., Kanigel, A., and Hayat, A. (2023). Ultrafast low-jitter optical response in high-temperature superconducting microwires. Appl. Phys. Lett. 122, 1. <https://doi.org/10.1063/5.0150805>.
191. Amari, P., Kozlov, S., Recoba-Pawlowski, E., Velluire-Pellat, Z., Jouan, A., Couëdo, F., Ulysse, C., Briatico, J., Roditchev, D., Bergal, N., et al. (2023). Scalable nanofabrication of high-quality YBa<sub>2</sub>Cu<sub>3</sub>O<sub>7-δ</sub> nanowires for single-photon detectors. Phys. Rev. Appl. 20, 044025. <https://doi.org/10.1103/PhysRevApplied.20.044025>.
192. Atikur Rahman, M., Rahaman, M.Z., and Samuddoha, M.N. (2015). A review on cuprate based superconducting materials including characteristics and applications. Am. J. Phys. Appl. 3, 39–56. <https://doi.org/10.11648/j.apja.20150302.15>.
193. Ghosh, S., Jangade, D.A., and Deshmukh, M.M. (2022). Nanowire bolometer using a 2D high-temperature superconductor. Nanotechnology 34, 015304. <https://doi.org/10.1088/1361-6528/ac9684>.
194. Romano, P., Riccio, M., Guarino, A., Martucciello, N., Grimaldi, G., Leo, A., and Nigro, A. (2018). Electron doped superconducting cuprates for photon detectors. Measurement 122, 502–506. <https://doi.org/10.1016/j.measurement.2018.02.010>.
195. Armitage, N.P., Fournier, P., and Greene, R.L. (2010). Progress and perspectives on electron-doped cuprates. Rev. Mod. Phys. 82, 2421–2487. <https://doi.org/10.1103/RevModPhys.82.2421>.
196. Long, Y., Zhao, L., Zhao, B., Qiu, X., Zhang, C., Fu, P., Wang, L., Zhang, Z., Zhao, S., Yang, Q., and Wang, G. (2006). Femtosecond optical response of electron-doped superconductor La<sub>2-x</sub>Ce<sub>x</sub>CuO<sub>4</sub>. Phys. C Supercond. 436, 59–61. <https://doi.org/10.1016/j.physc.2005.12.056>.
197. Charpentier, S., Arpaia, R., Gaudet, J., Matte, D., Baghdadi, R., Löfwander, T., Golubev, D., Fournier, P., Bauch, T., and Lombardi, F. (2016). Hot spot formation in electron-doped PCCO nanobridges. Phys. Rev. B 94, 060503. <https://doi.org/10.1103/PhysRevB.94.060503>.
198. Avella, A., Buonavolontà, C., Guarino, A., Valentino, M., Leo, A., Grimaldi, G., de Lisio, C., Nigro, A., and Pepe, G. (2016). Disorder-sensitive pump-probe measurements on Nd 1.83 Ce 0.17 CuO 4±δ films. Phys. Rev. B 94, 115426. <https://doi.org/10.1103/PhysRevB.94.115426>.
199. Ejnæs, M., Cirillo, C., Salvoni, D., Chianese, F., Bruscino, C., Ercolano, P., Cassinese, A., Attanasio, C., Pepe, G.P., and Parlato, L. (2022). Single photon detection in NbRe superconducting microstrips. Appl. Phys. Lett. 121, 262601. <https://doi.org/10.1063/5.0131336>.
200. Soltan, S., Albrecht, J., and Habermeier, H.-U. (2004). Ferromagnetic/superconducting bilayer structure: A model system for spin diffusion length estimation. Phys. Rev. B 70, 144517. <https://doi.org/10.1103/PhysRevB.70.144517>.

201. Przylapski, P., Komissarov, I., Paszkowicz, W., Dluzewski, P., Minikayev, R., and Sawicki, M. (2004). Magnetic properties of La 0.67 Sr 0.33 MnO<sub>3</sub>/YBa<sub>2</sub>Cu<sub>3</sub>O<sub>7</sub> superlattices. *Phys. Rev. B* 69, 134428. <https://doi.org/10.1103/PhysRevB.69.134428>.
202. Andersson, E., Arpaia, R., Trabaldo, E., Bauch, T., and Lombardi, F. (2020). Fabrication and electrical transport characterization of high quality underdoped YBa<sub>2</sub>Cu<sub>3</sub>O<sub>7</sub>- $\delta$  nanowires. *Supercond. Sci. Technol.* 33, 064002. <https://doi.org/10.1088/1361-6668/ab807e>.
203. Pena, V., Sefrioui, Z., Arias, D., Leon, C., Santamaria, J., Varela, M., Pennycook, S.J., and Martinez, J.L. (2004). Coupling of superconductors through a half-metallic ferromagnet: Evidence for a long-range proximity effect. *Phys. Rev. B* 69, 224502. <https://doi.org/10.1103/PhysRevB.69.224502>.
204. Pepe, G.P., Parlato, L., Marrocco, N., Pagliarulo, V., Peluso, G., Barone, A., Tafuri, F., Uccio, U.S.d., Miletto, F., Radovic, M., et al. (2009). Novel superconducting proximized heterostructures for ultrafast photodetection. *Cryogenics* 49, 660–664. <https://doi.org/10.1016/j.cryogenics.2009.02.002>.
205. Parlato, L., Ejrnaes, M., Nasti, U., Arpaia, R., Taino, T., Bauch, T., Myoren, H., Sobolewski, R., Tafuri, F., Lombardi, F., and Cristiano, R. (2017). Investigation of Dark Counts in Innovative Materials for Superconducting Nanowire Single-Photon Detector Applications. In *Photon Counting Applications, 10229 Photon Counting Applications*, pp. 69–74. <https://doi.org/10.1117/12.2267647>.
206. Arpaia, R., Ejrnaes, M., Parlato, L., Cristiano, R., Arzeo, M., Bauch, T., Nawaz, S., Tafuri, F., Pepe, G.P., and Lombardi, F. (2014). Highly homogeneous YBCO/LSMO nanowires for photoresponse experiments. *Supercond. Sci. Technol.* 27, 044027. <https://doi.org/10.1088/0953-2048/27/4/044027>.
207. Litombe, N.E.-S. (2015). *Nanopatterning and Transport Properties of Cuprate Superconductors*. PhD Thesis (Harvard University).
208. Sochnikov, I., Shaulov, A., Yeshurun, Y., Logvenov, G., and Bozović, I. (2010). Large oscillations of the magnetoresistance in nanopatterned high-temperature superconducting films. *Nat. Nanotechnol.* 5, 516–519. <https://doi.org/10.1038/NNANO.2010.111>.
209. Liang, R., Bonn, D.A., Hardy, W.N., and Broun, D. (2005). Lower critical field and superfluid density of highly underdoped YBa<sub>2</sub>Cu<sub>3</sub>O<sub>6+x</sub> single crystals. *Phys. Rev. Lett.* 94, 117001. <https://doi.org/10.1103/PhysRevLett.94.117001>.
210. Ramshaw, B.J., Day, J., Vignolle, B., LeBoeuf, D., Dosanjh, P., Proust, C., Taillefer, L., Liang, R., Hardy, W.N., and Bonn, D.A. (2012). Vortex lattice melting and H c 2 in underdoped YBa<sub>2</sub>Cu<sub>3</sub>O<sub>y</sub>. *Phys. Rev. B* 86, 174501. <https://doi.org/10.1103/PhysRevB.86.174501>.
211. Mori, Z., Tadokoro, M., Zulhairi, Z., Doi, T., Koba, S., Higo, S., and Hakuraku, Y. (2001). Micropatterning of NdBa<sub>2</sub>Cu<sub>3</sub>O<sub>7</sub> thin films using a KrF excimer laser. *Supercond. Sci. Technol.* 14, 45–49. <https://doi.org/10.1088/0953-2048/14/1/308>.
212. Tinkham, M. (2004). *Introduction to Superconductivity* (Courier Corporation).
213. Pashitskiĭ, É., Vakaryuk, V., Ryabchenko, S., and Fedotov, Y. (2001). Temperature dependence of the critical current in high-T c superconductors with low-angle boundaries between crystalline blocks. *Low Temp. Phys.* 27, 96–102. <https://doi.org/10.1063/1.1353699>.
214. Ohmukai, M., Fujita, T., and Ohno, T. (2001). The temperature dependence of critical current in YBa<sub>2</sub>Cu<sub>3</sub>O<sub>7-d</sub> thin films deposited on MgO by an eclipse PLD. *Braz. J. Phys.* 31, 511–513. <https://doi.org/10.1590/S0103-97332001000300027>.
215. Borsig, F. (2015). *Magnetic Field Resilient Superconducting Circuit Elements for Majorana Parity Detection* (Delft University of Technology). Master Thesis.
216. Datesman, A.M., Schultz, J.C., Cecil, T.W., Lyons, C.M., and Lichtenberger, A.W. (2005). Gallium ion implantation into niobium thin films using a focused-ion beam. *IEEE Trans. Appl. Supercond.* 15, 3524–3527. <https://doi.org/10.1109/TASC.2005.849029>.
217. Matsumoto, K., and Mele, P. (2009). Artificial pinning center technology to enhance vortex pinning in YBCO coated conductors. *Supercond. Sci. Technol.* 23, 14001. <https://doi.org/10.1088/0953-2048/23/1/014001>.
218. Barnes, P.N., Kell, J.W., Harrison, B.C., Haugan, T.J., Varanasi, C.V., Rane, M., and Ramos, F. (2006). Minute doping with deleterious rare earths in YBa<sub>2</sub>Cu<sub>3</sub>O<sub>7</sub>- $\delta$  films for flux pinning enhancements. *Appl. Phys. Lett.* 89, 012503. <https://doi.org/10.1063/1.2219391>.
219. Birlik, I., Erbe, M., Freudenberg, T., Celik, E., Schultz, L., and Holzapfel, B. (2010). Flux pinning improvement of YBCO superconducting films with BaZrO<sub>3</sub> nanoparticles prepared by chemical solution deposition method. *J. Phys. Conf. Ser.* 234, 12004. <https://doi.org/10.1088/1742-6596/234/1/012004>.
220. Maeda, H., Tanaka, Y., Fukutomi, M., and Asano, T. (1988). A new high-Tc oxide superconductor without a rare earth element. *Jpn. J. Appl. Phys.* 27, L209. <https://doi.org/10.1143/JJAP.27.L209>.
221. Hegmann, F., and Preston, J. (1993). Origin of the fast photoresponse of epitaxial YBa<sub>2</sub>Cu<sub>3</sub>O<sub>7</sub>- $\delta$  thin films. *Phys. Rev. B* 48, 16023–16039. <https://doi.org/10.1103/PhysRevB.48.16023>.
222. Sobolewski, R. (1998). *New Developments in High Temperature Superconductivity: Proceedings of the 2nd Polish-US Conference Held a Wrocław and Karpacz, Poland, 17–21 August 1998* (Springer), pp. 100–122.
223. Haldar, S., Sehrawat, A., and Balasubramanian, K.B. (2024). Modelling Response Time Contrasts in Superconducting Nanowire Single Photon Detectors. <https://doi.org/10.48550/arXiv.2403.07299>.
224. Rall, D. in *Journal of Physics: Conference Series*. 042029 (IOP Publishing).
225. Chang, J., and Esmaeil Zadeh, I. (2023). Superconducting single-photon detectors get hot. *Nat. Nanotechnol.* 18, 322–323. <https://doi.org/10.1038/s41565-023-01334-1>.
226. Bo, H., Ren, T., Chen, Z., Zhang, M., and Xie, Y. (2019). Enhancing superconductivity of ultrathin YBa<sub>2</sub>Cu<sub>3</sub>O<sub>7</sub>- $\delta$  films by capping non-superconducting oxides. *Chin. Phys. B* 28, 067402. <https://doi.org/10.1088/1056-28/6/067402>.